Spectroscopic Determination of Magnetic Fields in Pulsed-Power and High-Energy-Density Plasmas

Y. Maron, *Fellow, IEEE*, R. Doron, M. Cvejić, E. Stambulchik, D. Mikitchuk, C. Stollberg, T. Queller, E. Kroupp, G. Rosenzweig, B. Rubinstein, S. Biswas, V. Bernshtam, O. Nedostup, V. Litmanovich, V. Fisher, A. Starobinets, A. Fruchtman, *Senior Member, IEEE*, A. Fisher, V. Tangri, J. L. Giuliani, A. L. Velikovich, A. Dasgupta, *Senior Member, IEEE*, I. E. Ochs, E. J. Kolmes, M. E. Mlodik, S. Davidovits, N. J. Fisch, and M. D. Johnston

Abstract— We review spectroscopic methods developed for the determination of magnetic fields in high-energy-density (HED) plasmas. In such plasmas, the common Zeeman-splitting magnetic-field diagnostics are often impeded by various broadening mechanisms of the atomic transitions. The methods described, encompassing atomic transitions in the visible and ultraviolet spectral regions, are applied to the study of imploding plasmas (in a Z-pinch configuration) with and without pre-embedded magnetic fields, relativistic-electron focusing diodes, and plasma-opening switches. The measurements of the magnetic field in side-on observations of cylindrical-plasma configurations that are local in the radial direction despite the light integration along the chordal lines of sight are discussed. The evolution of the magnetic-field distributions obtained, together with the measurements of the plasma temperature and density, allows for studying the plasma dynamics, resistivity, and pressure and energy balance. In particular, for the Z-pinch, an intriguing question on the current flow in the imploding plasma was raised due to the observation that the current during stagnation mainly flows at relatively large radii, outside the stagnation region. For the premagnetized plasma implosions, all three components of the magnetic field (azimuthal, axial, and radial) were measured, yielding the evolution of the current flow and the efficiency of the axial field compression, as well as the relation between the geometry of the field and the plasma rotation, found to develop in this configuration. The measurements in the relativistic electron diode are used to quantify the shielding of the magnetic field by the plasmas in the diode. Also described are the experimental and theoretical investigations of a nondiffusive fast penetration of magnetic field into a low-density plasma (in the plasma-opening-switch configuration).

Index Terms— Electron and ion Diodes, line-shape analysis, magnetic-field measurements, plasma opening switch (POS), plasma spectroscopy, polarization spectroscopy, pulsed-power systems, Z-pinch.

Y. Maron, R. Doron, M. Cvejić, E. Stambulchik, D. Mikitchuk, C. Stollberg, T. Queller, E. Kroupp, B. Rubinstein, V. Bernshtam, O. Nedostup, V. Litmanovich, V. Fisher, A. Starobinets, and A. Fisher are with the Faculty of Physics, Weizmann Institute of Science, Rehovot 7610001, Israel (e-mail: yitzhak.maron@weizmann.ac.il).

G. Rosenzweig was with the Faculty of Physics, Weizmann Institute of Science, Rehovot 7610001, Israel. He is now with MKS Instruments, Inc., Wilmington, MA 01887 USA.

S. Biswas was with the Faculty of Physics, Weizmann Institute of Science, Rehovot 7610001, Israel. He is now with the Institute of Advanced Study in Science and Technology, Guwahati, Assam 781035, India.

A. Fruchtman is with the Faculty of Physics, Weizmann Institute of Science, Rehovot 7610001, Israel, and also with the Holon Institute of Technology, Holon 5810201, Israel.

V. Tangri, J. L. Giuliani, A. L. Velikovich, and A. Dasgupta are with the Plasma Physics Division, Naval Research Laboratory, Washington, DC 20375 USA.

I. E. Ochs, E. J. Kolmes, M. E. Mlodik, S. Davidovits, and N. J. Fisch are with the Department of Astrophysical Sciences, Princeton University, Princeton, NJ 08540 USA.

M. D. Johnston is with the Sandia National Laboratories, Albuquerque, NM 87185 USA.

Color versions of one or more figures in this article are available at https://doi.org/10.1109/TPS.2023.3296561.

Digital Object Identifier 10.1109/TPS.2023.3296561

I. INTRODUCTION

THE determination of magnetic fields (B-fields) is of fundamental importance for the understanding of the operation of numerous pulsed-power and high-energy-density (HED) systems. First and foremost, knowledge of the magnetic field distribution is the only way to determine the current density distribution in the plasma [1]. Knowledge of the evolution of the magnetic-field spatial distribution is thus essential for determining the distributions of the plasma resistivity and the ohmic heating, for understanding the plasma dynamics through the $\boldsymbol{j} \times \boldsymbol{B}$ forces (where $\boldsymbol{j}$ is the current density vector), and for assessing the energy and pressure balance [1], [2], [3].

The two most common spectroscopic methods for the B-field determination are based on: 1) the splitting of emission or absorption lines in the plasma due to the Zeeman effect and 2) the change of an external light-beam polarization due to the Faraday rotation (the external beam is weak enough to have no effect on the plasma properties). Another spectroscopic approach is applicable for the cases of low-beta plasma (the beta parameter is the ratio of the plasma pressure to the magnetic-field pressure), where the ion acceleration is driven by a magnetic field gradient [4], [5], allowing for inferring the magnetic field distribution from the time-dependent ion velocity.

Each of the two common methods has its challenges and limitations. For the particular plasma conditions typical to HED systems, the Zeeman-splitting magnetic-field diagnostics are often impossible. The high densities and

high ion velocities result in broad spectral line-shapes that smear out the Zeeman-split patterns, even when polarization techniques are employed for the suppression of the π Zeeman components of the spectrum. For the Faraday-rotation method, the rotation of the plane of polarization of an electromagnetic wave passing through a plasma is proportional to $\int n_e \vec{B} d\vec{l}$, where n_e is the electron density and l is the coordinate along the line of sight (LoS) (e.g., [6], [7]). Therefore, Faraday rotation requires knowledge of the electron density at all locations along the light propagation and is also an integrated measurement over the line of view, along which usually both B and n_e vary, which might lead to ambiguous interpretation of the data. Moreover, in chordal measurements in imploding plasmas, reconstructing the magnetic-field radial distribution requires assuming a cylindrical symmetry, which is usually unpredictable and is rather far from reality and thus may lead to substantial errors, see, for example, the discussion in [8]. For completeness, also mentioned is the proton beam deflectometry diagnostics (e.g., [9], [10], [11], [12], [13], [14]) that requires means for proton beam generation and integration of the effects of B and the electric field E on the proton trajectory over the entire proton path.

This review, following the presentation in the ICOPS 2021 minicourse, focuses on Zeeman-effect-based spectroscopic methods useful for HED conditions. The progress in measuring the magnetic fields in a variety of pulsed-power systems and the implication of these measurements to the understanding of the underlying physics is described. A discussion that also includes the measurements of other key parameters, namely, the electron and ion temperature and the turbulent and rotational ion motion that accompanied the B-field measurements, is given in a recent publication [15].

This review is organized as follows: it starts with a brief description of the Zeeman effect and demonstrates the difficulties in applying the common Zeeman-split diagnostics for HED conditions. Then, the use of the Zeeman effect for determining time-dependent magnetic-field distributions in pulsed-power systems, namely, Z-pinch implosions, a laser-produced plasma plume under an externally applied magnetic field, a relativistic self-magnetic-pinch diode, and magnetized plasma compression (MPC), is discussed. Also presented are B-field measurements in plasma opening switches (POSs), based on observing the ion dynamics. The measurements described are in the visible-UV band, encompassing plasma densities in the range of 10^{14}–10^{19} cm^{-3}.

II. CHALLENGES USING THE ZEEMAN EFFECT IN HED CONDITIONS

Consider an electric dipole transition between levels that can adequately be described in the LS approximation. The magnetic-field-induced splitting ΔE_{Zeeman} (both for the upper and the lower levels of the transition) in the weak-field approximation, i.e., when the perturbation due to the magnetic field is small compared to the fine-structure energy separations, is

$$\Delta E_{\text{Zeeman}} = g_{\text{LSJ}}\mu_B\,M_J\,B \tag{1}$$

where M_J is the projection of the total angular momentum J of the given state on the direction of the magnetic field B, μ_B
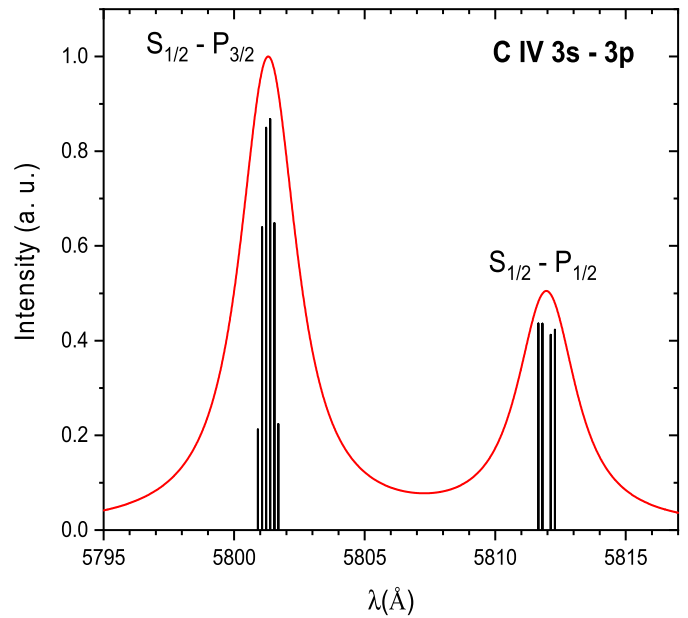

Fig. 1. Zeeman effect of the C IV $3s$–$3p$ doublet, calculated for a magnetic field of 1.5 T and convolved with Voigt profile due to a 0.3-Å full-width at half-maximum (FWHM) Doppler-Gaussian ($T_i = 4$ eV) and a 2.5-Å Lorentzian ($n_e = 5 \times 10^{17}$ cm^{-3}). Also shown is the Zeeman pattern with no broadening.
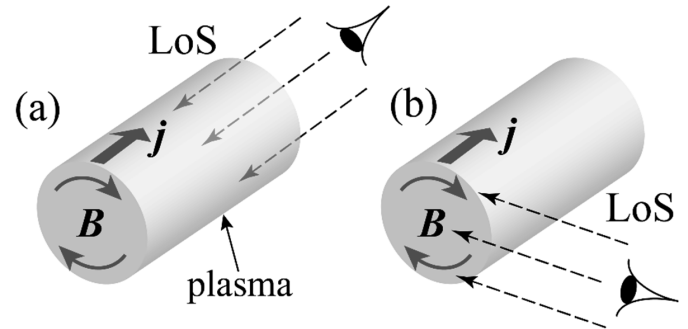

Fig. 2. Observation directions for obtaining LoSs that are (a) perpendicular and (b) parallel to B. Note that for the latter, the LoS is parallel to B only for the outermost radius of the line emission used.

is the Bohr magneton, and g_{LSJ} is the Landé g factor, given (neglecting the relativistic corrections) by

$$g_{\text{LSJ}} = \frac{J(J+1) + S(S+1) - L(L+1)}{2J(J+1)} \tag{2}$$

where S and L, respectively, are the total spin and the orbital momentum of the radiator. Note that $\Delta E_{\text{Zeeman}} \sim \mu_B B \sim 10^{-4} B$ (ΔE_{Zeeman} is in eV and B in T) and is independent of the transition energy. Thus, for $B = 1$ T, $\Delta E_{\text{Zeeman}} \sim 10^{-4}$ eV and the induced splitting can be measured in the visible-UV region. However, for $B = 10^4$ T, $\Delta E_{\text{Zeeman}} \sim 1$ eV and the splitting can be practically measured using X-ray transitions.

For the high plasma densities and high ion velocities in pulsed-power systems, smearing out of the Zeeman splitting due to Stark and Doppler broadenings is likely. In Fig. 1, the limitation of the Zeeman-split diagnostics due to the Stark broadening is demonstrated. The figure shows the Zeeman pattern of the C IV $3s$–$3p$ doublet transition for $B = 1.5$ T,
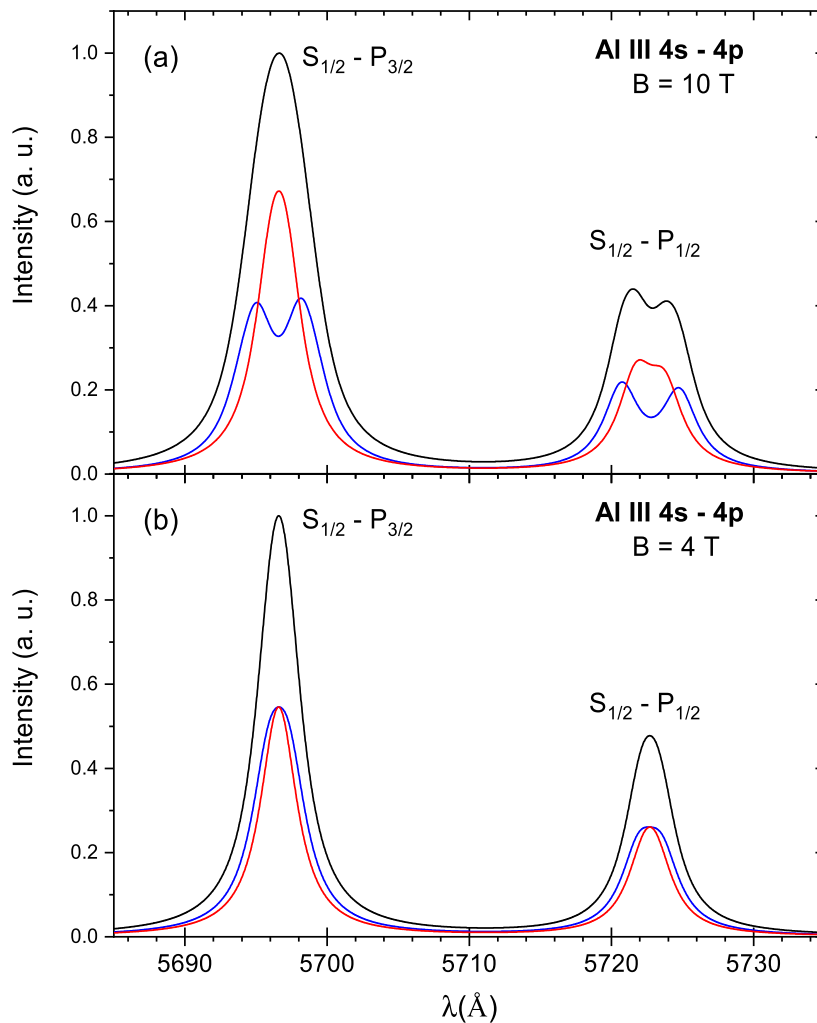
Fig. 3. Simulation of the Al III $4s$–$4p$ doublet assuming LoS perpendicular to $\boldsymbol{B}$: total emission (black); π (red); and σ (blue) linear polarizations for $n_e = 6 \times 10^{17}$ cm^{-3} and for (a) $B = 10$ T and (b) $B = 4$ T. (b) Intensities of the π and σ Zeeman components are peak normalized to highlight the linewidth differences.

assuming Doppler broadening due to $T_i = 4$ eV, convolved with a 2.5-Å Lorentzian that corresponds to a Stark broadening for $n_e \sim 5 \times 10^{17}$ cm^{-3}; the latter completely smears out the splitting. A similar difficulty may arise due to a large Doppler broadening. Therefore, progress in the B-field measurements for HED plasmas requires extending the spectroscopic diagnostics to conditions in which the Zeeman-split pattern is not resolvable. A discussion on the application regimes and limitations of the methods that extend the Zeeman-based spectroscopy is given in [16]. We now summarize the progress in the B-field measurements using these methods and the impact of the findings on the understanding of pulsed-power systems.

III. POLARIZATION-BASED ZEEMAN SPECTROSCOPY IN Z-PINCHES

In this section, we describe B-field measurements employing two methods that utilize the polarization properties of the Zeeman components. The first method is applicable for an LoS that is perpendicular to $\boldsymbol{B}$ and the second for an LoS that is parallel to $\boldsymbol{B}$, i.e., for a cylindrical geometry requiring end-on and side-on observations, respectively (see Fig. 2).

A. Line-of-Sight Perpendicular to B

For an observation perpendicular to $\boldsymbol{B}$, the π and σ Zeeman components are of orthogonal linear polarizations. To facilitate the Zeeman-splitting analysis, researchers traditionally use polarization measurements to remove the π component. This is demonstrated in Fig. 2(a) that presents the simulation of the Al III $4s$–$4p$ doublet spectrum for $B = 10$ T and $n_e = 6 \times 10^{17}$ cm^{-3}, together with the shapes of the π and σ polarizations. The removal of the π polarization allows the σ components to reveal a measurable splitting. However, for a lower B-field, this technique becomes inapplicable, as demonstrated in Fig. 2(b). In this case, the polarization properties of the line emission can still be utilized to measure B by detecting the different contributions to the line shape of the π and σ Zeeman components. As clearly shown in Fig. 3(b), the orthogonally polarized spectral lines have different line widths. Since this width difference is proportional to the B-field magnitude, it can be used for the field diagnostics.

The method of the width comparison of the π and σ polarizations was used, to the best of our knowledge, for the first measurement of the B-field in an imploding Z-pinch
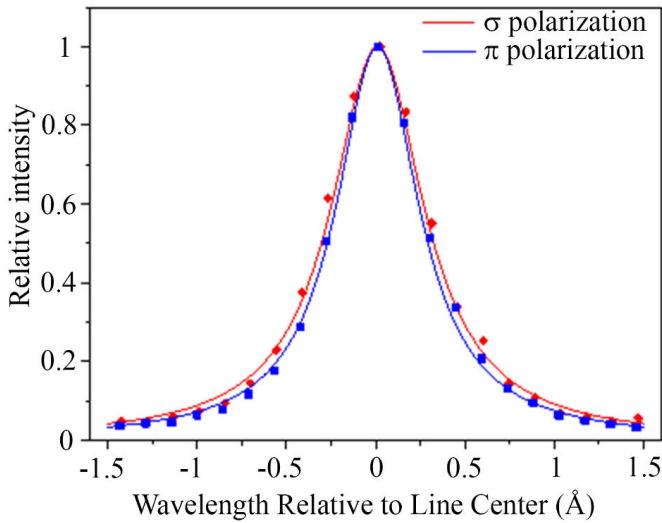
Fig. 4. Example of the profiles for the π and σ polarizations of the O IV 3063.5-Å line measured during the implosion at $t = 480$ ns after the current discharge; the time of the plasma stagnation on axis is 620 ns. Each data point is obtained by averaging over 20 discharges. The uncertainties are given by the size of the data points. The FWHMs of the Lorentzian fits are 0.56 ± 0.01 Å (π) and 0.62 ± 0.01 Å (σ), giving $B = 1.8 \pm 0.3$ T. The uncertainty in the FWHM is determined from the difference between the widths of profiles fitted to the upper or lower bounds of the data points. Reproduced from [17], with the permission of AIP Publishing.

plasma [17]. In that work, the radial distribution of the azimuthal B-field was measured as a function of time during the implosion of a CO_2 puff driven by a $\sim$300-kA, 1.6-μs current pulse. End-on observations (LoS parallel to the z-axis and perpendicular to the azimuthal magnetic field B_θ) of the plasma shell were employed. Since the linewidth difference was rather small, a reliable measurement required a high signal-to-noise ratio; thus, an averaging of the measurements for each polarization over a number of discharges was required. An example of the measured line shapes recorded in the π and σ polarizations, demonstrating the width difference used for the B-field determination, is given in Fig. 4.

The measured time-resolved magnetic-field distributions, presented in Fig. 5 [17], demonstrate the rise of B due to the compression and the rise of the circuit current. As the plasma radially implodes, the azimuthal B-field diffuses radially inward into the plasma and is compressed together with the plasma. By fitting the solution of the diffusion equation of B to the measured time-dependent radial distributions of B, the conductivity of the plasma was determined and found to be nearly in agreement with the Spitzer value that was estimated from the electron temperature and density determined spectroscopically for the same plasma [18], [19].

Using the magnetic field radial distributions obtained in this work [17], together with earlier measurements in similar experiments of the distributions of the charge states, electron density, and ion velocities [20], it became possible to determine the distribution of the ion radial acceleration due to the $j \times B$ forces. To this end, considered was a gas element residing at $r_0 = r(t_0)$, where t_0 is the time the gas element is encountered by the leading edge α of the imploding plasma and is ionized into singly charged ions. The radial position $r(t)$

of this fluid element at time t is given by

$$r(t) = r(t_0) + \int_{t_0}^{t} v_\alpha\big(r(t'), t'\big) dt' \tag{3}$$

where $v_\alpha(r(t'), t')$ is the measured radial velocity of ions of the fluid element α; the data in [20] allowed for following the velocity rise of a fluid element as it ionizes into higher charge states, since the time it is encountered by the leading edge of the imploding plasma. The magnetic force acting on an ion in the fluid element is then

$$\begin{aligned} F_R(r, t) &= \frac{1}{n_\alpha(r, t)} J_z(r, t) \cdot B_\theta(r, t) \\ &= \frac{Z_\alpha(t)}{n_e(r, t)} J_z(r, t) \cdot B_\theta(r, t) \end{aligned} \tag{4}$$

where n_α is the ion density and $Z_\alpha(t)$ is the time-dependent effective charge of the fluid element considered. $F_R(r, t)$ gives the ion radial velocity V_α that would have resulted only from the $j \times B$ forces by

$$V_\alpha(r(t), t) = \int_{t_0}^{t} \frac{d\tau}{m_i} F_R(r(\tau), \tau) \tag{5}$$

where m_i is the ion mass.

An example of the histories of V_α and v_α for a fluid element that is encountered by the leading edge of the imploding plasma at $t = 470$ ns and $r = 1.35$ cm is shown in Fig. 6(a). Given in Fig. 6(b) are the time-dependent total acceleration of the fluid element a_{tot} and the acceleration $a_{j \times B}$ due to the magnetic force, both obtained from the velocity curves in Fig. 6(a). The time-dependent ion acceleration due to the thermal pressure gradient is then obtained by subtracting the contribution of the $j \times B$ forces from the total radial acceleration of the ions, both shown in Fig. 6(b). It is seen that until $t \approx 520$ ns, when the ions are still relatively far from the outer boundary of the plasma, the radial acceleration due to the $j \times B$ force is negligible, i.e., the ion acceleration is caused by the thermal pressure. The magnetic pressure becomes dominant [namely, $a_{j \times B} \sim a_{\text{tot}}$, see Fig. 6(b)] at later times, when the particles are highly ionized and are located closer to the outer boundary of the plasma. For example, at $t \approx 535$ ns, the O V ions, mainly accelerated by the magnetic pressure, are located at $r = 1.1$ cm, where the outer boundary R_0 is at 1.15 cm. This analysis, if repeated for different fluid elements, demonstrates the use of the magnetic field measurements in obtaining a complete r, t mapping of the thermal pressure across the plasma shell.

The measured B-field and plasma properties were also used to study the history of the magnetic-field energy coupling to the plasma, by comparing the energy deposition and dissipation rates in the plasma and by assessing the pressure terms as a function of radius and time [19]. This analysis allowed for concluding that $\sim$2/3 of the energy deposited in the plasma up to the last stage of the implosion is imparted to the plasma radial flow, while the rest of the energy is converted into internal energy and radiation. In addition, the measured magnetic-field distribution allowed for determining the energy terms in the implosion phase, which helped explaining the propagation of an ionization wave in the imploding
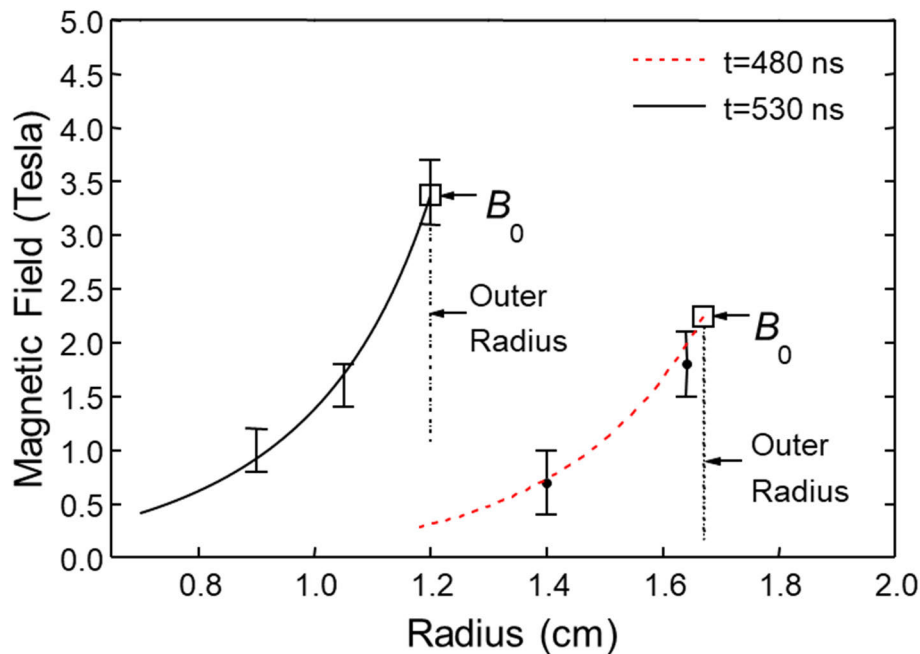
Fig. 5. Magnetic-field radial distribution in the imploding plasma column at different times. The fitting curves are based on the solution of a 1-D magnetic-field diffusion equation for each time using a plasma conductivity that is constant over the plasma shell, where $\sigma = 3.1 \times 10^4$ and 2.7×10^4 $\Omega^{-1}\text{m}^{-1}$ for $t = 480$ and 530 ns, respectively (i.e., 140 and 90 ns, respectively, before the stagnation on axis). The time of stagnation is $\approx$620 ns. B_0 is the field magnitude at the outer edge of the plasma. Reproduced from [17], with the permission of AIP Publishing.

plasma [21] and, thus, the time-dependent radial distribution of the ionic charge states in the plasma [20].

The measurements described above were successful only for radii > 8 mm and up to 90 ns prior to stagnation. At smaller radii or at times closer to stagnation, the Stark and Doppler broadenings were too dominant to allow for the determination of the linewidth difference of the two polarizations.

B. Line-of-Sight Parallel to B

When the LoS is parallel to the magnetic field, only the σ Zeeman components are collected, and the light is circularly polarized: right-handed for $\sigma+$ and left-handed for $\sigma-$. The different polarizations of the σ Zeeman components allow each of these components to be recorded separately using a quarter-wave plate and a linear polarizer, e.g., see [22]. The wavelength separation between these two components is used for the field determination, as demonstrated in Fig. 7 and described in the studies of astrophysics, e.g., [23], [24] and laboratory plasmas, e.g., [22], [25], [26], [27], [28], [29], [30]. This method is nearly unaffected by emission-line opacities since it relies on the components relative shift rather than on the line shapes. When applicable, this method is the most sensitive (among the Zeeman-effect-based methods) to the magnetic field [16]. Indeed, this technique was instrumental in recent measurements that significantly improved our understanding of the Z-pinch stagnation and magnetized-plasma compression (see the following).

In these measurements, B was obtained throughout the entire plasma shell and throughout stagnation [31], [32]. Chordal LoSs were used to observe the Zeeman effect as a function of radius. A formidable difficulty in measuring B as a function of radius over the entire imploding plasma is due to the integration of the spectra along the LoS. Generally, this means that Abel inversion of the data is required, which in imploding plasma experiments, is likely to lead to misleading results due to the common azimuthal nonuniformity of the plasma and the low signal-to-noise ratio in the data. Thus, it is essential to find ways to perform local measurements in radius, i.e., avoiding the need for Abel inversion. In addition, due to the irreproducibilities of pulsed-power experiments, determining B in various radii simultaneously in a single discharge is desirable. In the work, described in [31] and [32], both challenges were addressed. This was achieved by taking advantage of the naturally formed gradients in the plasma conditions that lead to the variation of the ionic charge state with radius, as in [20]. Measuring the field by utilizing an emission line of a certain charge state, while looking chordally at the outermost region in which the charge state is present, ensures a line of view parallel to the field and at a region limited in the radial and azimuthal dimensions, i.e., yielding B at the radius of this region (demonstrated in Fig. 8). Moreover, since line shapes of transitions of different charge states can be recorded simultaneously, observing lines from several charge states (each by looking at the outer region of the respective emission) provides the magnetic field magnitude at several radii, yielding the field radial distribution in a single experiment.

An example of a measurement, where the $\sigma+$ and $\sigma-$ separation allows for obtaining the B distribution in spite of the overwhelming Stark and Doppler broadenings, is presented in Fig. 9, where recorded is the O III 3791.26-Å $(2s^2 2p3s\ ^3P_2 - 2s^2 2p3p\ ^3D_2)$ line and the O VI 3811.35-Å $(1s^2 3s\ ^3S_{1/2} - 1s^2 3p\ ^3P_{3/2})$ line. Moreover, the
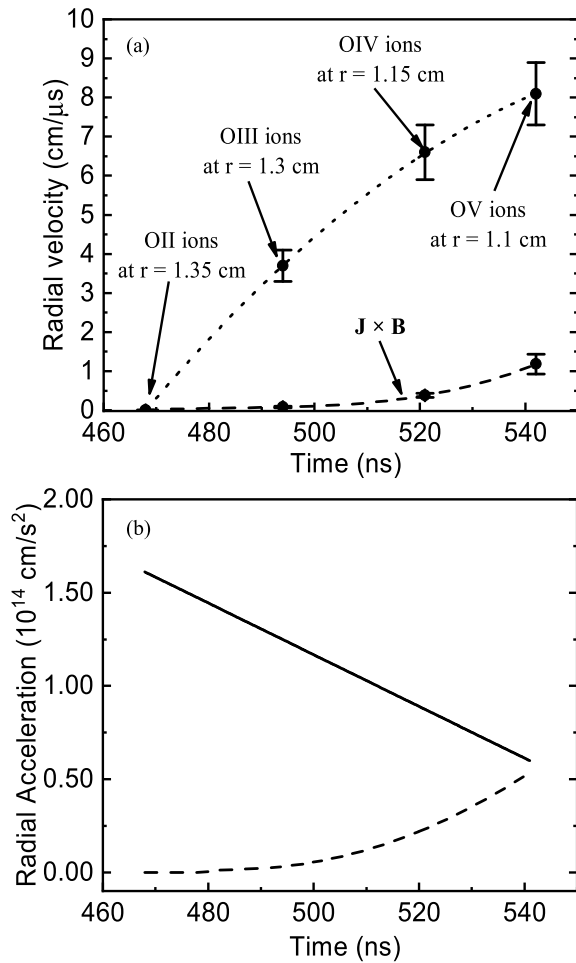
Fig. 6. Velocity history [17] of a fluid element that is encountered by the leading edge of the imploding plasma at $t = 470$ ns (i.e., 150 ns before plasma stagnation) and $r = 1.35$ cm, obtained from the measured [20] radial velocities of the various charge state ions across the plasma shell. The dotted line is a smooth monotonic curve through the data points. The dashed line is the calculated accumulated contribution of the $j \times B$ forces in the plasma to the time-dependent velocity of the same fluid element. The arrows indicate the times and the corresponding radial locations at which this fluid element is dominated by the respective ionization stages. (b) Total radial acceleration as a function of time of the fluid element (solid line), together with the radial acceleration only due to the $j \times B$ forces (dashed line). Both curves are obtained by derivation of the velocity curves given in (a). Reproduced from [17], with the permission of AIP Publishing.

Lorentzian-Stark contribution to the line shape, which is the dominant line broadening mechanism, enables to determine simultaneously the radial density distribution.

It should be noted that the Zeeman splitting pattern of $\sigma+$ and $\sigma-$ in general is asymmetric, as is clearly seen for the O VI transition shown in Fig. 9. Asymmetry will also appear if the magnetic field is not exactly parallel to the LoS (see Section VI-B). An additional minor source of asymmetry is the deviation from the weak-field approximation, when the Zeeman B-splitting is not negligible compared to the fine structure. However, in HED plasmas, other broadening mechanisms (instrumental, Doppler, and Stark), together with the common noise in the data, usually obscure the asymmetry. In cases where the signal-to-noise ratio is sufficiently high to allow the detection of the asymmetry, one could use the

Zeeman pattern convolved with other broadening mechanisms to determine B with higher accuracy.

Using $B_\theta = (\mu_0 I / 2\pi R)$, where B_θ is the azimuthal field value measured at the radius R and I is the axial current within a cylinder of this radius, each such data point yields the total current flowing within the respective radius, producing a current radial distribution from which the current density can be derived. The radial distribution of the B-field throughout stagnation [31], [32] showed that the peak field remains at a radius much larger than the stagnation radius at all times. The current flowing through the stagnating plasma is found to be a small fraction of the total current. This constitutes the first direct confirmation of the conclusion, originally obtained from pressure and energy balance considerations [33], that the magnetic field pressure and energy play a small role in the plasma stagnation. In that work [33], gas puff and wire array stagnations were shown to be consistent with an exploding shock model based on the implosion velocities, the radiation processes, and the plasma turbulence. Indeed, in a subsequent paper, the spectroscopic data from the stagnation were reanalyzed by accounting for the density fluctuations resulting from the turbulence [34]. The density fluctuations were taken from the theories of compression of fluid turbulence in plasma that is inviscid on the time scales of the compression [35], [36], [37], [38], [39]. The analysis of the data accounting for the self-consistent density fluctuations [34] demonstrated better concordance of the overconstrained spectroscopic measurements, while also substantially lowering the inferred mean density at stagnation.

Further measurements of the radial distributions of the intensities of various charge-state transitions enabled, due to observations of various subtleties in the distribution, a simultaneous determination of the magnetic field at several radial locations throughout stagnation, and, in particular, down to small radii [40], [41]. These measurements confirmed the conclusions stated above regarding the small fraction of the current flowing in the stagnated plasma and also provided a large dataset, along the pinch column, that allowed for comparison to magnetohydrodynamics (MHD) simulations [42].

Recent detailed measurements in a small-scale Z-pinch experiment [43], employing the radially resolved B-field diagnostics that were also time-resolved, revealed a remarkable dynamics of the current. It was found that in a certain part of the pinch column, the discharge current undergoes an abrupt transition during the stagnation; from an initial stage where it is carried down to the very small radius of the stagnating plasma to a stage where most of the current flows in an low-density plasma (LDP) residing at much larger radii, while the stagnating plasma continues its implosion [45], [44]. This observation might be related to indications of possible current restrikes in wire-array Z-pinches inferred from imaging techniques [46], [47], [48], as well as to current flowing in a trailing plasma of wire array [46], [47], [48], [49], [50], [51], [52], and gas-puff Z-pinches [14], [15], [30], [31], [32], [53].

Meanwhile, a model based on advection was then proposed [54] to explain this unintuitive bounce of the current channel and plasma motion. In this model, certain velocity
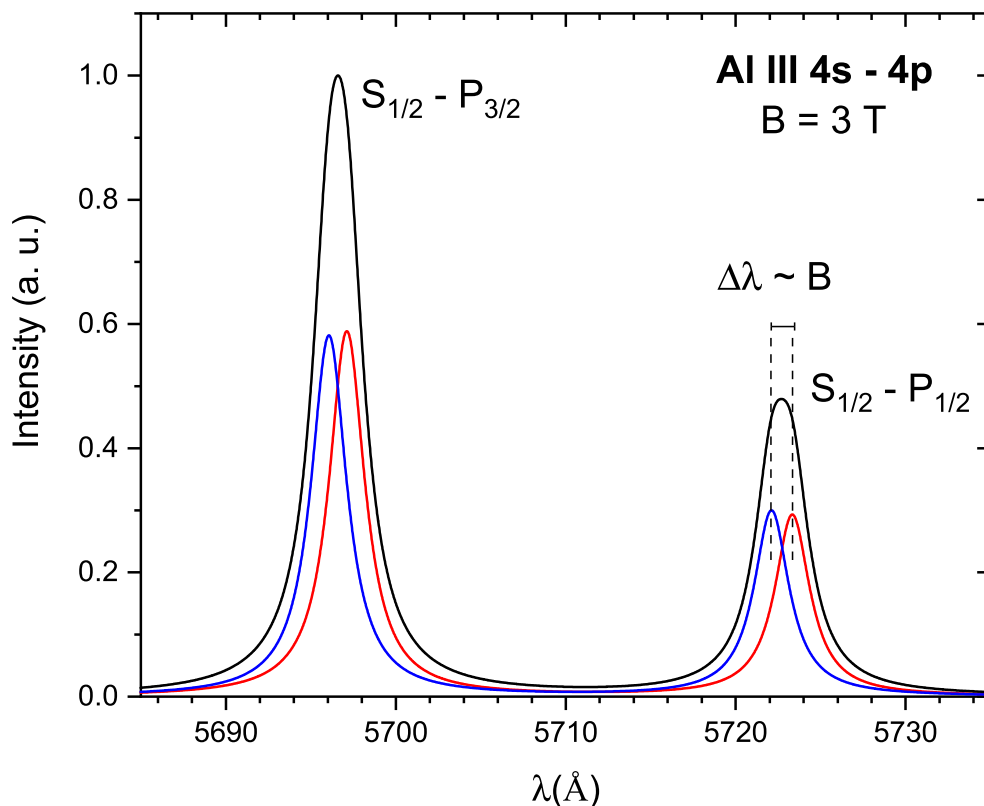
Fig. 7. Simulation of the Al III $4s$–$4p$ doublet at $B = 3$ T and $n_e = 5 \times 10^{17}$ cm^{-3}, assuming an LoS parallel to $\boldsymbol{B}$: total emission (black), σ^+ (blue), and σ^- (red)—Zeeman polarizations.
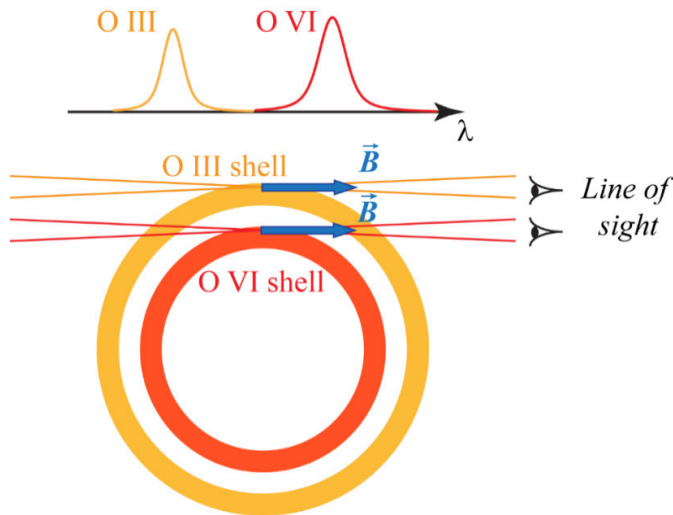

Fig. 8. Schematic of measurements of the B-field radial distribution, utilizing the emission lines of different charge states that are abundant within different radii. Observing the line emission from the outermost radius, in which each charge-state emits, provides radially resolved data without the need for the Abel inversion. It also ensures viewing parallel to $\boldsymbol{B}$.

Fig. 9. Analysis of the O III 3791.26-Å and of the O VI 3811.35-Å lines. The measured line shapes of each of the σ polarizations are fitted with Voigt profiles, from which the Zeeman effect is obtained. The Zeeman-split patterns are shown by the vertical bars. The separation between the polarized-line positions is twice the wavelength shift, $\Delta\lambda$, obtained from the energy separation in (1). The O III line was recorded from $r = 8$ mm and the O VI from $r = 5$ mm, yielding $B = 7.1 \pm 0.6$ and 5.5 ± 0.5 T, respectively.

profiles, satisfying the condition $d/dr(|v_r|/r) < 0$ (where v_r is the plasma radial velocity and r is the plasma radial position), were shown to cause a fast current transport outward, while the plasma implosion continues.

Fig. 10 shows a spectral image of the small-scale Z-pinch at stagnation, demonstrating the simultaneous measurement of the B-field at different radii using spectral lines from different charge states (O III and O IV). In order to accurately measure
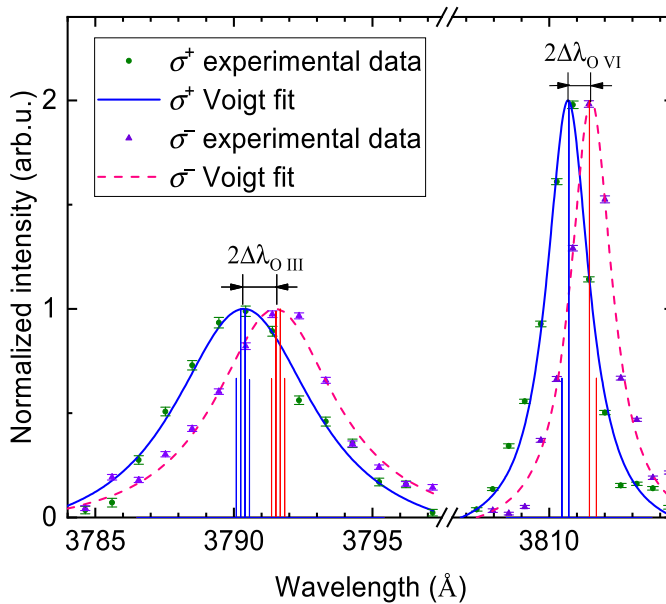
the separation between the σ Zeeman components, the two components must be recorded simultaneously on different parts of the detector, which was achieved by imaging the
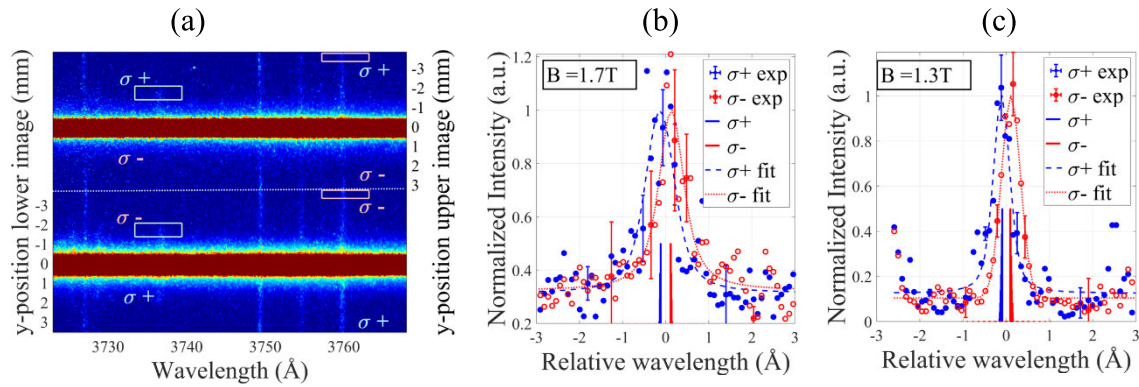
Fig. 10.   (a) Spectral image of the chordally integrated spectrum of the small-scale Z-pinch at stagnation. (b) Line shapes of the O IV $3p$–$3d$ transition at 3736.85 Å, recorded at different polarizations ($\sigma+$ and $\sigma-$ at the upper and lower part of the detector, respectively), obtained from the lineout of the spectral image taken from $r = (-1.90 \pm 0.35)$ mm (marked by the white rectangles), together with the best fits. The peak separation between the $\sigma+$ and $\sigma-$ yields $B = 1.7$ T. The zero-density, Doppler-free Zeeman pattern is plotted at the bottom. (c) Same as (b) for the O III $3s$–$3p$ transition at 3759.87 Å, yielding $B = 1.3$ T at $r = (-3.55 \pm 0.21)$ mm.
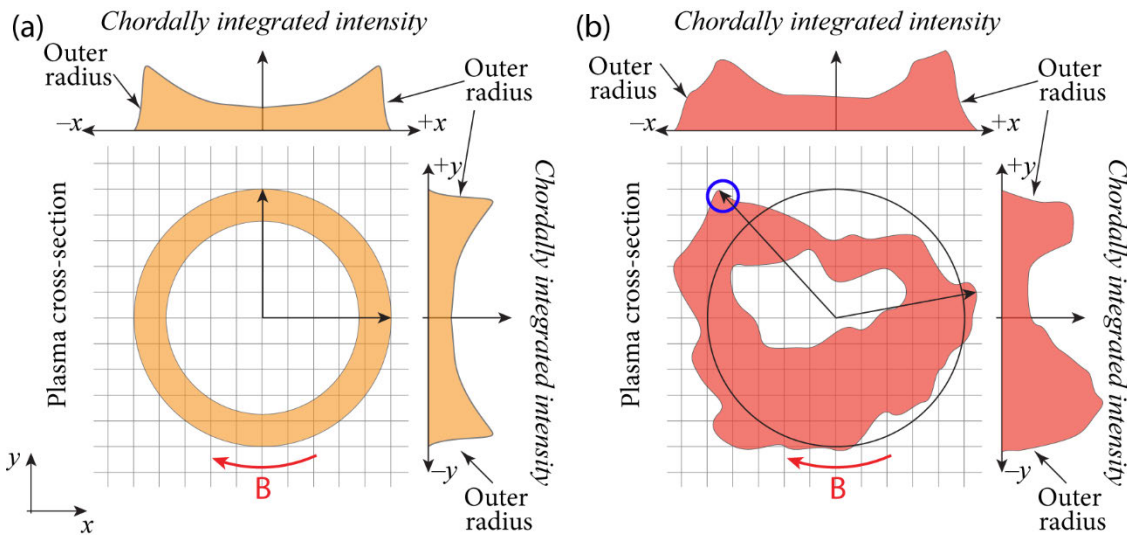

Fig. 11.   Illustration of a plasma column cross section and the chordally integrated intensity distribution from two orthogonal directions, for two cases. (a) Column for which the outer edge of a given line emission is azimuthally symmetric and (b) outer edge is not azimuthally symmetric, causing the chordally integrated intensity distribution from two orthogonal directions to be significantly different. In both cases, the plasma is assumed to be uniform and $\boldsymbol{B} = B_\theta$. The emission from the small volume circled by blue cannot be used for the measurement, when viewed from either orthogonal directions in (b), see text.

plasma emission with the two different polarization properties on two different regions of the detector (upper and lower, see Fig. 10). Note that since in this experiment the entire plasma cross section was imaged, B is parallel and antiparallel to the LoS for $y > 0$ and $y < 0$, respectively. This causes the opposite polarization properties denoted on the image.

The measurements presented in Fig. 10 for $r = 1$ and 3 mm were taken close to the time of stagnation and after the current redistribution. Indeed, the measured $B(r)$ does not follow the expected $1/r$ decay, resulting from the current flow through the entire plasma cross section, namely, between $r = 1$ mm and $r = 3$ mm.

We mention here that polarization spectroscopy was used to determine B at the outer regions of a gas-puff implosion [22], [55]. Also, the observation of the Zeeman splitting [56] was used to determine B in the outside region of an imploding liner in a $\sim$20 MA experiment on the Z machine and next to the return current conductor in a hybrid X-pinch [57].

C. Identifying the Outermost Radius of a Line Emission

Two conditions are crucial for the correct implementation of the method that deems Abel Inversion unnecessary, discussed in Section III-B: 1) the observed volume, identified as the outer edge of the line emission, is located at the radius associated with the chordal LoS (i.e., located at the point of the minimal distance between the chord and the pinch axis) and 2) the LoS is parallel to B in the observed volume. While these conditions are readily achieved for an azimuthally symmetric plasma column, their fulfillment in an asymmetric plasma poses a difficulty resulting from the fact that the data are chordally integrated, as clarified in Fig. 11. The figure schematically presents the cross section of a plasma column emitting an optically thin spectral line for two cases: 1) an azimuthally symmetric plasma and 2) an asymmetric plasma. Also shown are the respective chordally integrated intensity images observed from orthogonal directions. In case 1), the two orthogonal images are identical, verifying its azimuthal symmetry, and ensuring that a spectrum recorded close to

the outer edge of a given line emission originates from the outermost radius of that emission, where the LoS is parallel to B_θ. In case 2), however, using a spectrum from a point close to the outermost edge of a given emission guarantees neither a measurement from a known radius nor a view at a direction that is parallel to B. This is illustrated, for example, in Fig. 11(b), where it is shown that, indeed, using a spectrum from the volume marked by a blue circle is inadequate for both orthogonally viewing spectroscopic systems. Fig. 11 also demonstrates that it is desirable to examine the azimuthal asymmetry of the outer-edge emission of any utilized emission by the employment of two orthogonal spectrally imaging systems. It should be emphasized that for determining the location of the outermost radius of a given line emission, no complete azimuthal symmetry is required for the entire column cross section (as required for Abel inverse transform), but only a weaker condition of an azimuthal symmetry of the outermost location of the utilized line emission.

In the case of irreproducible experiment that also lacks azimuthal symmetry, it is necessary to employ a few side-on spectroscopic systems. Each imaging system observes the spectra across the entire diameter of the plasma from a different direction. By choosing optically thin lines, it becomes sufficient to image only from one side of the implosion. By comparing the chordally integrated intensity distributions (see Fig. 11) obtained from different directions, it is possible to determine the deviation of the radial position of the outermost emission of a given transition from an azimuthal symmetry. This allows for obtaining the radial position of the outermost emission that is viewed by a certain spectroscopic system, and the angle between the observation direction and B, with a reasonable accuracy (here, a quasi-concentric B_θ is assumed). Knowledge of the deviation of the viewing direction from a parallel observation to B allows for calculating the correct Zeeman emission pattern for the true angle, which is then accounted for in inferring the magnetic field.

In our experiments, we used simultaneously two side-on spectroscopic systems viewing the column from orthogonal directions. Repeated measurements allowed us to confirm that the outermost radius is azimuthally symmetric to within ± 0.25 mm (compared to ~ 5-mm column radius). This verification also ensured that the deviation of the direction of view from the parallel direction to $\boldsymbol{B}$ was negligible.

Doppler shifts due to the plasma implosion provide additional information on the azimuthal symmetry of the system. In side-on observations, for an azimuthally symmetrical plasma, the LoS through the plasma edge exhibits no Doppler shift (since the imploding-plasma motion is perpendicular to the direction of observation), whereas the LoS through the diameter (parallel to the motion) yields the largest Doppler shifts. For an imploding annulus, the red- and blue-shifted emissions from each side yield a line splitting [20]. Thus, for a uniform radial implosion, the line emission image along the diameter yields an elliptical shape, as demonstrated in Fig. 12. Deviations from an elliptical shape, which can be detected particularly for chords close to the LoS through the diameter (where the Doppler shifts are the largest), provide information on deviations from a cylindrical symmetry. It is
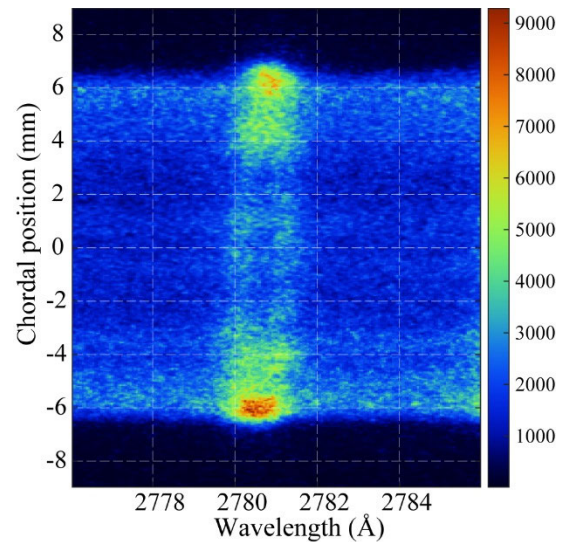

Fig. 12. Chordally integrated spectral image of the O V 2781.01-Å line along the entire diameter of the cylindrical plasma. Doppler shifts due to implosion make the image elliptical along the diameter. Doppler shifts due to rotation [58] tilt the "ellipse."

noted that the spectral image shown in Fig. 12 was recorded in a Z-pinch experiment with pre-embedded axial magnetic field (see Section VI), where the imploding plasma column is also rotating [58], resulting in a tilted ellipse.

IV. MEASUREMENTS OF B HAVING AN ARBITRARY DIRECTION

The two polarization-based methods described above require that the B-field has a dominant direction. However, when the magnetic-field direction varies in time or over spatial scales that are integrated over due to the limited diagnostic-system resolutions, polarization techniques are inapplicable. In such cases of "nondirectional" fields, to the best of our knowledge, the only known available spectroscopic approach is that based on the comparison of line shapes of different fine-structure components of the same multiplet, suggested in [59].

The principle of this method is based on the fact that the different fine-structure components of the same atomic multiplet undergo different Zeeman splittings, while the other line-broadening mechanisms, namely, the Stark and the Doppler effects, and the instrumental broadening, are practically identical for the two components. The method is demonstrated in Fig. 13, where the Al III doublet, $4s\,^2S_{1/2}$–$4p\,^2P_{1/2}$(5696.6 Å) and $^2S_{1/2}$–$^2P_{3/2}$ (5722.7 Å), is simulated for $B = 8$ T; with the 1/2 –1/2 component being wider. Therefore, if these two multiplet components are recorded simultaneously, the difference between the line shapes, that is only due to the magnetic field, can be used for the field determination. Since the diagnostics does not rely on the emission polarization properties, it is applicable to nondirectional magnetic fields. Also, since opacity effect (if present) acts in the opposite direction, i.e., the broadening caused by self-absorption is larger for the stronger and narrower component ($^2S_{1/2}$–$^2P_{3/2}$), if the plasma opacity is not accounted for, the measurement yields a lower limit for the magnetic field.
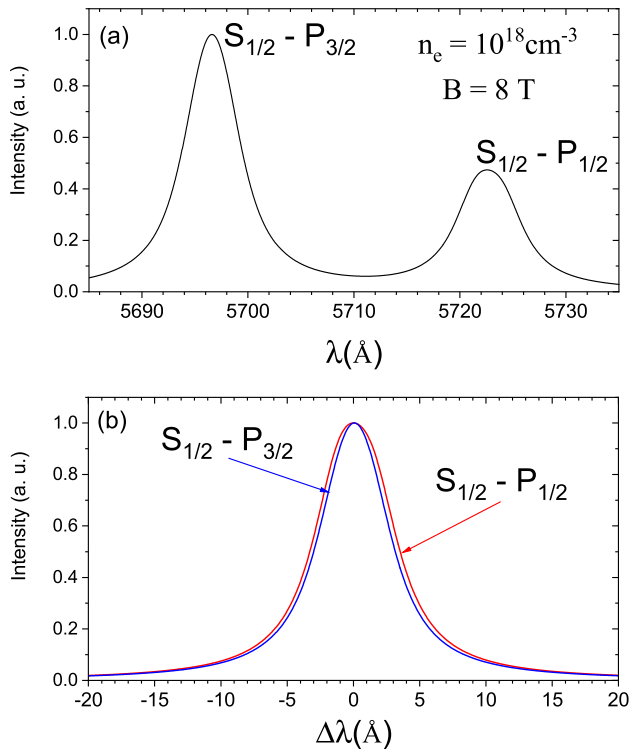
Fig. 13.   (a) Simulation of the Al III $4s$–$4p$ doublet for $n_e = 10^{18}$ cm^{-3} and $B = 8$ T. (b) Comparison between the peak-normalized line shapes of the two doublet components shows the difference in the line widths, revealing the presence of the magnetic field.

Fig. 14.   Al III $4s$–$4p$ doublet (5696 and 5722 Å) recorded from laser-produced plasma under applied B (squares). The calculated broadened spectrum (solid curve) that best matches the experimental data yields an electron density of 1.3×10^{18} cm^{-3} and $B = 15$ T. The dotted line represents the corresponding zero-density Zeeman pattern. The apparent structures at the top of the line shapes are believed to be due to the Zeeman-split pattern of LDP (and low Stark broadening) emission, superimposed on the much stronger high-density plasma emission.

In high-density plasmas, the two fine-structure components may significantly overlap. In such a case, a simple comparison of the multiplet line shapes for inferring the field, as shown in Fig. 13, is not possible. Nevertheless, the diagnostics are still useful by means of detailed line shape simulations [60] of the entire multiplet, also yielding information on n_e. In this approach, the Stark and Zeeman effects are assumed to be independent and the total line profile is the convolution of the Zeeman pattern and the Stark profile, assumed to be a shifted Lorentzian (e.g., an isolated-line shape calculated in the impact approximation [61]). This approach was demonstrated [59], [62] for measuring B and n_e in a laser-produced plasma plume under an externally applied magnetic field. An example of the measurement from [62] is given in Fig. 14.

V. B-Field Measurements in Relativistic Self-Magnetic-Pinch Diode

In high-current electron diodes, the self-generated magnetic field causes electron-beam focusing at the center of the anode [63], [64]. Plasma is formed all over the anode surface during and after the process of the beam focusing [65]. Knowledge of the beam current profile, which can be obtained from the B-field distribution, is required for understanding the pinch dynamics and for optimizing the diode performance. The magnetic field was determined in the anode plasma in the Sandia 10-MV, 200-kA electron beam diode [66], where the Zeeman effect in transitions of carbon ions present in the anode plasma was recorded, yielding the B-field in various radial positions near the anode surface.
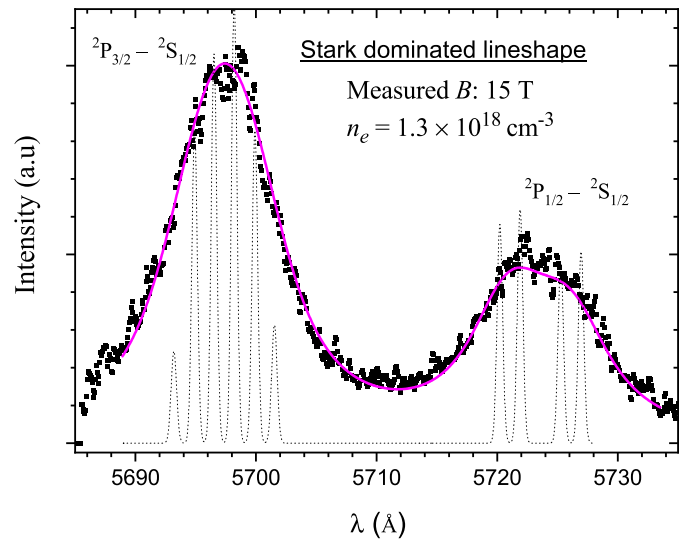
Also, for this diode [64], the radial distribution of B in the anode plasma for different distances from the anode surface was inferred [67]. Fig. 15 presents an example of the experimental data of the C IV $^3 S_{1/2}$–$^3 P_{1/2}$ component, recorded for different distances from the diode axis at 0.75 mm away from the anode surface. The fits of the line shape computations (also shown in Fig. 15) to the data yield both the B-field and the electron density from the Stark broadening.

In this work, the measured B-field as a function of distance from the anode surface allowed for quantitatively determining the shielding of the magnetic field in the anode plasma. It also allowed for fitting the variation of B with the distance from the anode surface (namely, from the vacuum gap across the plasma to the anode surface) to a solution of the diffusion equation, which yielded the plasma resistivity. The latter was found to be close to the Spitzer resistivity for this plasma, estimated using the electron temperature and charge-state distribution determined from line-intensity ratios [67].

The partial shielding of the magnetic field found in the relativistic self-magnetic-pinch diode is rather different from the findings in an ion-beam diode [68], obtained by the early Zeeman-based spectroscopic measurements. In the ion diode, the anode plasma was found to be fully penetrated by the magnetic field that rises during the current pulse, which allowed for determining the anode plasma resistivity and the diamagnetic effect of the electron Brillouin flow in the diode gap.

Fig. 16 shows the values of B_θ obtained for the various radial positions. It is seen that the B_θ values obtained from the C IV line are higher than those obtained from the Al III lines even though the spectrum of the two ions is collected by the same fiber focused at $z = 0.75$ mm. Indeed, it was shown that the intensity ratio of the C IV-to-Al III lines significantly
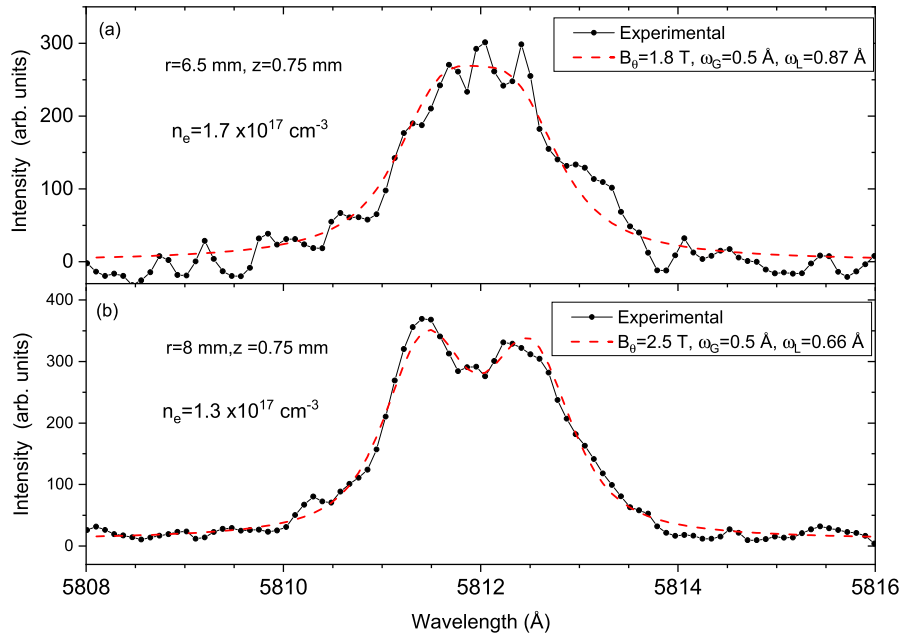
Fig. 15. C IV $3s$–$3p$ $^3S_{1/2}$–$^3P_{1/2}$ component from the region 0.5–1 mm from the anode surface, at different radii after inverse-Abel transformation. (a) $r = 6.5$ mm and (b) $r = 8$ mm. Dashed (red) curves are the simulated spectra obtained by convolving the Zeeman profile with the Stark and instrumental profiles. In the legend, B_θ, ω_L, and ω_G are the azimuthal magnetic field, the Stark FWHM, and the instrumental (Gaussian) FWHM used for the fit, respectively. Reproduced from [67], with the permission of AIP Publishing.
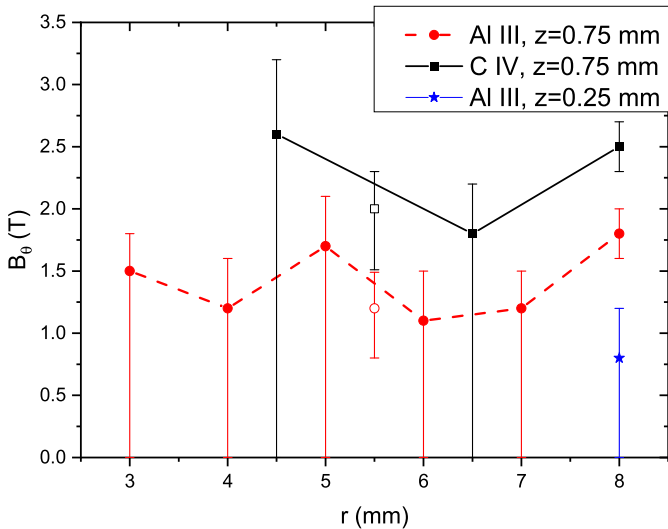

Fig. 16. Radial distribution of B_θ obtained from the fit of the shapes of the C IV $3s$–$3p$ $3S_{1/2}$–$3P_{1/2}$ (black square) and Al III $4s$–$4p$ $3S_{1/2}$–$3P_{1/2}$ (red circle) transitions. The data points at $r = 4.5$ mm and $r = 6.5$ mm for C IV are averages over the signals at $r = 4$ and 5 mm and $r = 6$ and 7 mm, respectively. Open symbols denote the average value of B_θ in the radial region at $4 \leq r \leq 7$ mm and $0.5 \leq z \leq 1$ mm. Reproduced from [67], with the permission of AIP Publishing.

increases with the distance from the anode (e.g., at $r = 4$ mm, from $\sim$0.1 at $z = 0.25$ mm to $\sim$0.4 at $z = 0.75$ mm). Thus, while the emissions of both Al and C are collected from the same field of view, the Zeeman effect of the C IV line reflects the B-field at a distance from the anode surface that is longer (within the field of view) than that of the Al III line. This means that the use of two different species provides some spatial resolution within the data collected by a single fiber. The lower B_θ toward the anode surface, seen in Fig. 16,

evidently demonstrates the stronger shielding of the magnetic field deeper into the plasma.

VI. Z-PINCH IMPLOSIONS WITH PRE-EMBEDDED AXIAL MAGNETIC FIELD

In a Z-pinch with a pre-embedded axial magnetic field or magnetized plasma compression (MPC), the plasma and the embedded axial field (B_{z0}) are compressed by the azimuthal magnetic field due to the axial current driven in the plasma. MPCs have been intensely studied during the last decade [30], [69], [70], [71], [72], [73], [74], [75], [76], [77], [78], [79], [80], [81] due to their importance for inertial confinement fusion (ICF) [69], [70], [71], [72], for the study of fundamental plasma physics [1], [15], and for experimental astrophysics [82]. The compression of both the plasma and axial magnetic field affects profoundly the implosion dynamics. Two such remarkable phenomena, recently discovered, are the redistribution of the axial current flow to large radii, where LDP resides [30] and self-generated plasma rotation [58].

A. Experimental Setup

Fig. 17(a) shows a schematic of the experimental and diagnostic setup. A cylindrical oxygen-puff shell with initial outer and inner radii of 19 and 7 mm, respectively, and mass $\sim$10 μg/cm, as determined by interferometry, prefills the A–K gap with a pre-embedded, quasistatic axial magnetic flux. B_{z0} is generated by a pair of Helmholtz coils placed outside the vacuum chamber, rising in $\sim$95 ms, to allow for the diffusion of B_{z0} into the vacuum chamber and the A–K gap. Subsequently, a pulsed current (rising to 300 kA in 1.6 μs) is driven through the gas, ionizes it, and generates an azimuthal magnetic field that compresses the plasma radially
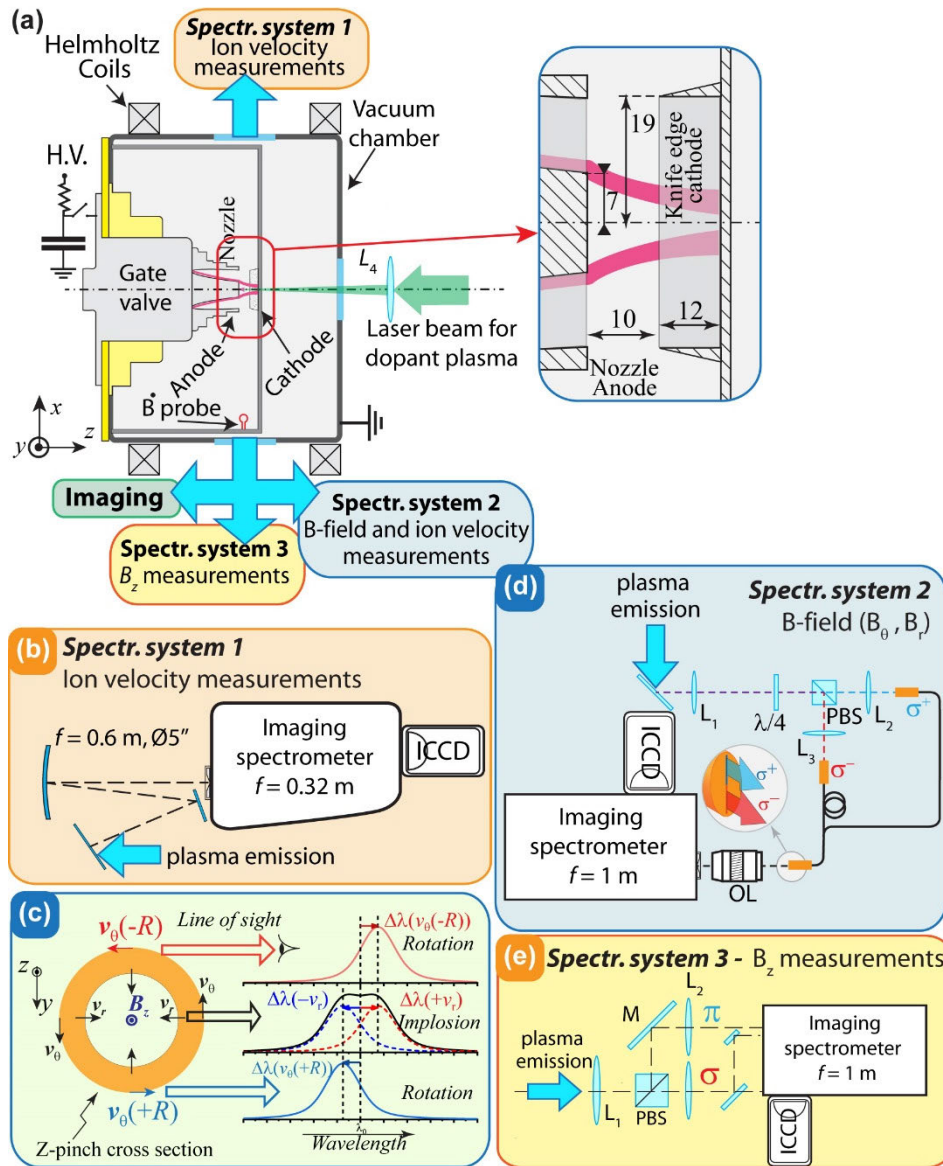
Fig. 17. (a) Schematic description of the experimental setup and spectroscopic systems for the magnetized plasma diagnostics. The inset shows the geometry of the electrodes in the vicinity of the A–K gap. (b) Spectroscopic system 1 used for the measurements of the ion velocities and plasma parameters. (c) Schematic of the spectroscopic measurements of rotation and the plasma implosion velocities. (d) Spectroscopic system 2 used for magnetic field measurements. (e) Spectroscopic system 3 used for the axial magnetic field measurements, see the text.

inward together with the embedded B_z field. An absolutely calibrated B-dot probe measures the total current. More details can be found in [30] and [58]. In [30], the Helmholtz coils were placed inside the vacuum chamber and were pulsed to give $B_{z0} = 0.4$ T.

Fig. 17 shows the diagnostic setup designed for acquiring spatially and temporally resolved data for simultaneous determination of the B-fields, the plasma parameters, and ion motion. It consists of three imaging spectroscopic systems. The LoS of all systems is perpendicular to the pinch axis, where the LoS of system 3 is perpendicular to the LoS of systems 1 and 2 [30], [83]. The radial distribution of the various parameters is obtained by taking advantage of the radial separation of the ion charge states during the implosion, as described in Section III-C [15], [17], [32], [58], [84].

B. B_θ Measurements

As shown in Fig. 17(a) and (d), the imploding plasma column is observed radially. The collected light passes through a quarter-wave plate that transforms the right-handed circularly (RHC) polarized and left-handed circularly (LHC) polarized components into orthogonal linear polarizations that are subsequently split using a polarizing beam splitter. Each of the two polarizations is then imaged on a separate linear array of 50 optical fibers. The light exiting the array is imaged along the entrance slit of a high-resolution (0.3 Å) imaging spectrometer; its output coupled to a gated (10 ns) intensified charge-coupled device (ICCD). This setup allows for a simultaneous recording of the two polarization components, emitted from the exact same plasma volume, on different parts of a single detector, with a spatial resolution of 0.3–0.7 mm

[which depends on the magnification ratio of f_{L1}/f_{L2}, see Fig. 17(d)] in the radial and axial directions.

In a magnetized plasma experiment, when B_θ is measured using the method for an LoS parallel to B (see Section III-B), one must consider that the B vector, in addition to the azimuthal component, can have axial and radial components, namely, $\boldsymbol{B} = B_\theta \hat{\theta} + B_z \hat{z} + B_r \hat{r}$.

While the B_z component, resulting from the initial B_{z0}, is present in the A–K gap throughout the Z-pinch implosion [30], [83], the B_r component is only formed as the implosion progresses. Since the B_z flux in the plasma column is compressed during the implosion, whereas in the (metal) electrodes, it is frozen at its initial radius, and a region near the electrodes, where the B_z-field lines are bent radially, is formed. Therefore, significant B_r values are possible only near the electrodes and in the late implosion stage. The details of the technique for the measurement of B_r, which carries an important role in the generation of the plasma rotation [58], will be given in a separate publication.

Thus, in general, in the magnetized plasma experiment, the B-field is not parallel to the LoS even for observations at the outermost radius of a utilized emission, and the data analysis becomes complex. However, except for the period at the beginning of the implosion and at stagnation, B_z at the outer plasma edge is much lower than B_θ, and thus, the influence of the B_z component on the B_θ determination is negligible [83].

Furthermore, the calculations show that if the presence of B_z (and/or B_r) components is not accounted for (i.e., analyzing the peak separation between the LHC and RHC line shapes assuming LoS parallel to B), the value obtained for B_θ is higher than the true B_θ [30], [58]. In the case of B_z and B_θ having comparable magnitudes, the line shapes in the LHC and RHC polarized channels become asymmetric. The analysis of such cases will be the subject of a future publication.

To illustrate the richness of the data extracted from a single measurement, an example of the data recorded by the diagnostic system shown in Fig. 17(d) is given in Fig. 18. The spectral recording shows the $\sigma+$ and $\sigma-$ Zeeman components of the O III 3791.26-Å and O VI 3811.35-Å transitions along the entire plasma diameter, allowing for the simultaneous determination of five quantities that are both radially resolved for two opposite azimuths and time-resolved. These quantities are: B_θ—obtained from the wavelength separation between the $\sigma+$ and $\sigma-$ Zeeman-induced shifts seen in the lineout at the outermost radius [30], [31], [32], v_θ—the azimuthal velocity (rotation velocity) obtained from the Doppler-line shifts of the lineouts at the outermost radii at the opposite azimuths [58], v_r—the radial velocity from the Doppler shift using the lineout at $y = 0$ [20], [58], n_e—the electron density from the Stark broadening obtained from the spectral shape of either the $\sigma+$ or $\sigma-$ components [60], [61], and T_e—the electron temperature from the line-intensity ratios of different transitions from the different charge states [85].

Studying the Z-pinch implosion with B_{z0} [30] revealed a phenomenon, where even a weak initially applied axial magnetic field can have a significant impact on the current distribution in the plasma. During the implosion, a large part
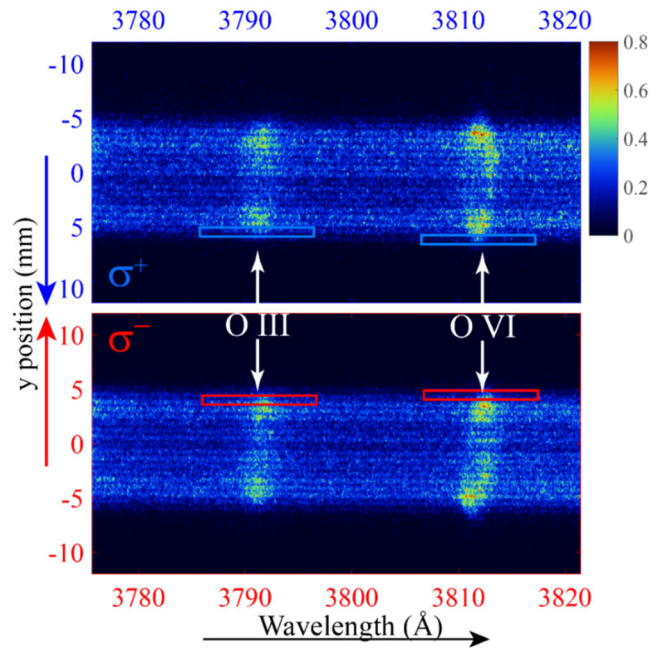

Fig. 18. Spectral image of the chordally integrated O III 3791.26-Å and O VI 3811.35-Å transitions for $B_{z0} = 0.26$ T. The upper- and lower-part show, respectively, the RHC and LHC polarizations along the plasma diameter, recorded on the same ICCD sensor. It is evident from the lateral intensity distribution that O VI resides at larger radii than O III. The blue and red rectangles show the position of the lineouts taken from the outermost radii of the emission of the O III and O VI lines at positive azimuth $(+y)$.

of the current is diverted from the imploding plasma to an LDP residing at large radii. These results were achieved by spectroscopic measurements of the azimuthal magnetic fields, as a function of space and time throughout the implosion [30], [83]. Systematic magnetic-field measurements were made utilizing the polarization-based spectroscopic technique for light emission viewed parallel to the magnetic field, as discussed in Section III-B. The results for $B_{z0} = 0.4$ T are summarized in Fig. 19. Using Ampère's law $\mu_0 I = 2\pi r B_\theta$, the measured B_θ evolution at the outer plasma radius r (defined at 20% of the peak emission-intensity radial distribution) of the main imploding argon plasma shows that only ~25% of the total current flows within this plasma. It was found that the majority of the current flows at large radii through a slowly imploding, LDP consisting of hydrocarbon impurities. In contrast, for $B_{z0} = 0$ (not shown here), the measured B_θ shows that the entire current flows within the imploding plasma shell. This finding indicates that the application of B_{z0} significantly affects the current distribution in the plasma, so that only a small part of the current flows through the imploding plasma. Furthermore, it was found that the fraction of the total current that flows in the imploding plasma decreases with a higher B_{z0} [30].

To explain this phenomenon, a model for the current distribution evolution that is based on the development of a force-free current flow [30], [86] in the peripheral, LDP was suggested. The phenomenon was also demonstrated in a numerical simulation [87].

This finding of the current escape to the peripheral plasma in the presence of B_z might be of paramount importance for
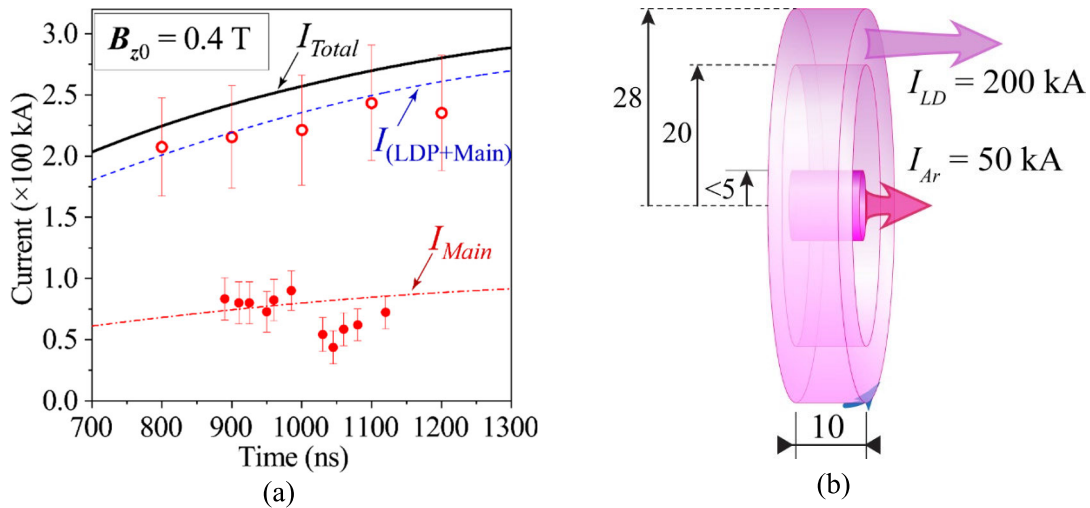
Fig. 19. (a) Evolution of the current flow in the main imploding argon plasma and in the slowly imploding, LDP present at large radii. (b) Cartoon of the results shown in (a). I_{LD} and I_{Ar} are, respectively, the current flowing in LDP and in the main argon plasma.

the ICF concept based on MPC, since the flow of the current at the larger radii impairs the implosion that compresses the liner and heats the magnetized-fuel plasma. In addition, the observed current redistribution can explain various not understood observations from other MPC experiments, see [15], [30], [73], [75], [76], [79], [80], [81], [88], [89], [90].

C. Diagnostics of B_z

Knowledge of the axial magnetic field (B_z) distribution and its evolution are essential for understanding the governing basic processes, such as the B-field diffusion, ohmic heating, implosion dynamics, energy balance, and the effect of the electrodes on the compression.

Presented here is a brief summary of the experimental determination of the B_z distribution near the plasma axis in oxygen-puff Z-pinch, throughout the magnetized plasma implosion, based on the polarization properties of the Zeeman effect [83], [91]. The measured values are then compared to the expected ones, assuming the B_z flux is conserved during the implosion and follows the evolution: $B_z(t) = B_{z0} (R_0/r(t))^2$, where R_0 is the initial radius of the gas-puff and $r(t)$ is the imploding plasma radius.

In determining B_z in the plasma shell, two major difficulties are encountered: 1) the need to distinguish between the axial and the azimuthal magnetic fields along the LoS and 2) the absence of light emission from the on-axis region of the nearly hollow cylindrical plasma column. To circumvent these difficulties, a dopant plasma is introduced in the central region of the cylinder, along the imploding plasma axis. Two schemes were employed: 1) generating a dopant plasma plume by a laser ablation ($\lambda = 512$ nm, $t_{pulse} = 7$ ns, and $E_{pulse} = 300$ mJ) of an Al-target attached to the anode and 2) introducing a small amount of CH_4 using a jet from a central nozzle. The spectral lines of the dopant plasma, which are different from those originating at the surrounding main (oxygen or argon) plasma, provide local information on B_z close to the axis.

At axial positions relatively close to the anode and at the early stage of the implosion, the relatively low density
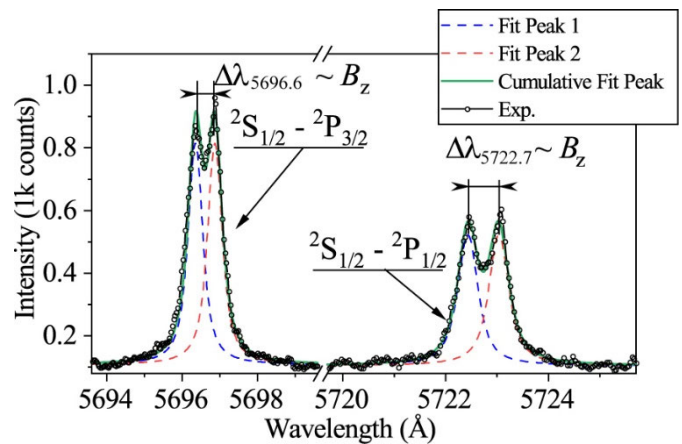

Fig. 20. Spectral lines of Al III $4s–4p$ ($\lambda = 5696.6$ and 5722.7 Å) from the laser dopant plasma, recorded at $t = -115$ ns (the stagnation is at $t = 0$) and $z = 7$ mm ($z = 0$ is the anode-nozzle surface) for $B_{z0} = 0.26$ T. The Zeeman-split pattern is clearly observed, yielding $B_z = (1.6 \pm 0.1)$ T.

of the expanding laser-ablated Al dopant plasma allows for observing the Zeeman-split pattern by selecting the σ Zeeman polarization (here, the line emission is viewed perpendicular to the axial magnetic field) components of the Al III $4s–4p$ ($\lambda = 5696.6$ and 5722.7 Å) transitions, as demonstrated in Fig. 20. At later times, when the dopant becomes embedded in a high-density plasma due to the compression by the imploding plasma, the Stark width smears out the Zeeman-split pattern, and therefore, B_z was determined [83] by detecting the linewidth difference between the π and the σ Zeeman components, as performed in [17] and described above in Section III-A. Farther away from the anode, where the Al-dopant presence is inhibited due to the imploding main plasma shell approaching the pinch axis, B_z was determined by utilizing the C IV $3s–3p$ ($\lambda = 5801.3$ and 5812 Å) transitions. To this end, a small amount of CH_4 gas was injected through a central nozzle. For $B_{z0} = 0.26$ T, the measurements were possible up to ~ 20 ns before stagnation (~ 700 ns after current initiation).
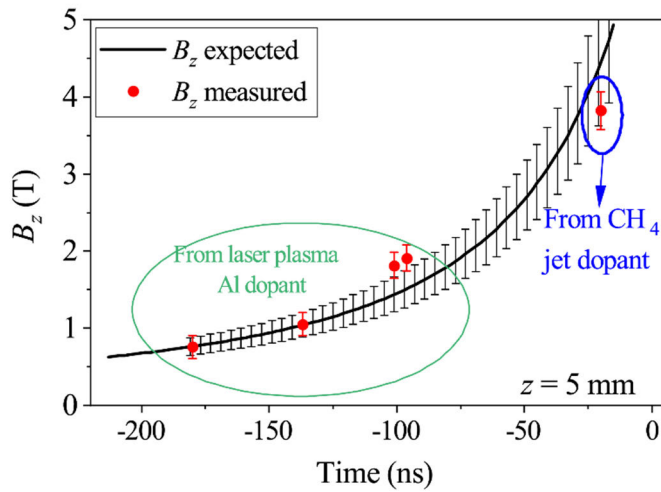
Fig. 21. Evolution of B_z at $z = 5$ mm. The curve represents the ideal magnetic flux compression, and the error bars on that curve are due to the uncertainty in the plasma radius.

Fig. 22. Schematic description of the ion separation. The B-field propagates at a speed of v_B. The light ion plasma (high Z/M) is reflected from the magnetic field front, acquiring a velocity that is twice v_B, whereas the heavy ion (low Z/M) plasma is penetrated by B acquiring velocities (depending on Z/M) that are lower than v_B.

Recording the shapes of the Al III and C IV lines from dopant plasma at different times during implosion, in separate shots, allowed for obtaining the time evolution of B_z. Fig. 21 shows that the measured values follow the curve of ideal magnetic flux compression, meaning that the axial magnetic field is ideally conserved within imploding plasma shell.

While the B_z flux is almost ideally conserved in the oxygen-puff experiment presented here, in a similar experiment with argon-puff, only ~50% of the B_z flux was conserved in the implosion [30], [83]. The reason for the different B_z flux conservation between the two experiments is presently studied and will be the subject of a future publication.

VII. MAGNETIC-FIELD PROPAGATION IN A LOW-DENSITY PLASMA (PLASMA-OPENING SWITCH CONFIGURATION)

Plasma pushing by magnetic field pressure, which is a dominant process in Z-pinches, was also expected to be the dominant process in POS [92], [93], [94], [95], [96], [97], [98]. However, following indications by probe measurements [95], [97], Zeeman-effect spectroscopic measurements with high spatial and temporal resolutions revealed that the magnetic field penetrates into the POS plasma in a nondiffusive manner, much faster than expected by the plasma resistivity [4], [5], [99], [100], [101], [102], [103], [104]. Here, observing the Zeeman effect in ionic line emission, by doping the plasma using laser evaporation techniques, Shpitalnik et al. [100] and Arad et al. [102] allowed for measurements that were local in 3-D.

Theories explaining the fast magnetic field penetration are based on the Hall-electric-field mechanism, shown to be capable of inducing the field penetration if the scale of the plasma nonuniformity is smaller than the ion skin depth, as indeed often occurs in the POS Low-Density Plasmas [105], [106], [107], [108], [109], [110], [111], [112]. The magnetic field then penetrates the plasma as a traveling wave. The mechanism of penetration is clearly demonstrated at the limit of motionless ions. In the POS experiments described above, however, the
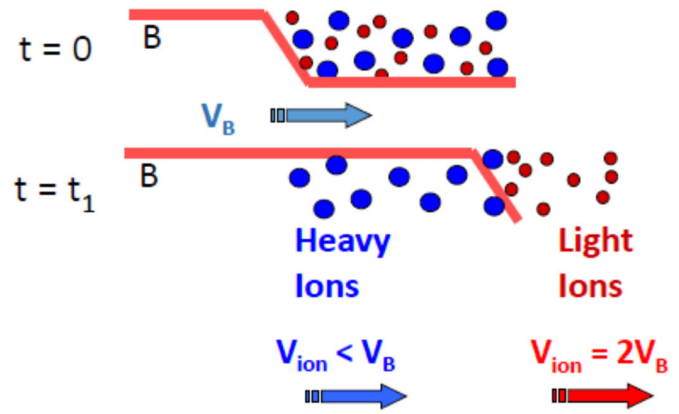
magnetic field penetration occurs while plasma motion is also significant [4], [5], [99], [100], [101], [102], [103], [104], [113], [114].

Further spectroscopic studies uncovered another remarkable phenomenon. It was found that the field penetration is accompanied by ion separation, where a high charge-to-mass ratio (Z/M) plasma (mainly protons) is pushed ahead, while a low Z/M plasma (mainly carbon ions) lags behind the magnetic piston, as schematically described in Fig. 22. The magnetic-field measurements allowed for demonstrating that most of the momentum imparted by the magnetic field pressure is given to the reflected light ions, and most of the dissipated magnetic field energy was converted into kinetic energy of these ions, even though their mass is only a small part of the total plasma mass [101], [103].

Subsequent studies [5], [113], to the best of our knowledge, provided a first experimental verification of the traveling-wave-like picture of the magnetic field and the associated electric potential hill propagating nondiffusively in the low-resistivity plasma of the switch, as described in the following. Obtaining such detailed information on the structure of the propagating magnetic field required measuring the magnetic field with a high sensitivity and with a submillimeter spatial resolution, which is close to the electron skin depth (350 μm), a scale that is significantly smaller than the few-millimeter width of the front of the penetrating magnetic field. Under the relevant plasma conditions, obtaining sufficiently high signal-to-noise ratio for a reliable analysis of Zeeman-dominated line-shape could not be achieved without compromising the spatial and temporal resolutions. Rather, the required resolution was achieved by developing a spectroscopic method for simultaneous measurements of the time evolution of the dopant ion-velocity and electron density across the magnetic-field front.

The diagnostic approach [5], [113] took advantage of the POS-plasma low-beta, where the electric force that accelerates the unmagnetized ions is equal to the magnetic force on the entire plasma, which is proportional to the magnetic field gradient. Thus, the ion velocity evolution can serve as a probe for the shape of the magnetic field. In the wave reference

frame, the dopant ions climb an electrostatic potential hill, and their total energy is conserved

$$\phi = \frac{m_i}{2Z_i e}\left(v_B^2 - \tilde{v}_i^2\right) \tag{6}$$

where $\tilde{v}_i$ is the ion velocity and ϕ is the electrostatic potential along the potential hill ($\phi = 0$ at the foot of the potential hill), both in the moving frame of the magnetic field, Z_i and m_i are, respectively, the ion ionization degree and mass, e is the elementary charge, and v_B is the magnetic-field propagation velocity.

The axial profile of the propagating magnetic-field front can now be calculated. The plasma is highly conductive, so the accelerating electric field can be approximated by $E_z = -(B/e\mu_0 n_e)(\partial B/\partial z)$ (e.g., [107]), where μ_0 is the vacuum permeability. The magnetic field is then given by

$$B^2(\phi) = 2e\mu_0 \int_0^\phi n_e(\phi')d\phi'. \tag{7}$$

Employing a laser blow-off technique, a $\sim$4-mm-wide, low-density (peak dopant ion density $< 1.5 \times 10^{13}$ cm^{-3} that is approximately an order of magnitude lower than the POS-plasma ion density) dopant column was injected into the plasma. A submillimeter spatial resolution (along the LoS) was then achieved by tracking the dopant-ion velocity—the parameter used for obtaining the electric potential [see (9)]—only at the center of the dopant column [5]. These time-dependent velocity measurements showed that the electric field accelerating the ions indeed propagates in the plasma as a traveling wave. Since all ions move under the same electric potential, the measured dopant-ion velocity allowed for calculating the dynamics of all ion species, and together with the spectroscopically determined plasma composition [115], for deriving self-consistently the electron density evolution that is also required for the magnetic-field determination (7). The electron-density evolution and its precise correlation with the ion velocity were also independently measured [113] and found to agree with the velocity-based density derivation, further assessing the traveling-wave nature of the propagating magnetic field.

The reconstruction of the electric potential and the shape of the magnetic field front with a resolution comparable to the electron skin depth advances the understanding of the plasma—magnetic-field interaction in the low-beta regime, as in this experiment. The measured width of the propagating magnetic-field front was used to determine the plasma resistivity [5]. These detailed data are also useful for comparison with simulations that account for the complex dynamics of multispecies plasmas, e.g., [112], [116], [117], [118], [119], [120], [121].

VIII. SUMMARY

The measurements of the magnetic-field distribution as a function of time and space in various pulsed power systems provide deep insight on the current flow and the plasma behavior and reveal a number of unpredicted phenomena. In particular, the observed evolution of the current distribution in imploding plasmas, both magnetized and unmagnetized, still lacks a rigorous theoretical description. We believe that extensive comparison between such detailed measurements and MHD modeling will be useful for better understanding of the observations, as well as for benchmarking theoretical modeling.

For the magnetized plasma implosion experiments, additional experimental efforts are required to better characterize the dynamics of the B_z compression and obtain more quantitative data on the relation between the field 3-D geometry along the plasma column and the plasma rotation.

REFERENCES

[1] J. L. Giuliani and R. J. Commisso, "A review of the gas-puff Z-pinch as an X-ray and neutron source," *IEEE Trans. Plasma Sci.*, vol. 43, no. 8, pp. 2385–2453, Aug. 2015.

[2] D. D. Ryutov, M. S. Derzon, and M. K. Matzen, "The physics of fast Z pinches," *Rev. Mod. Phys.*, vol. 72, no. 1, pp. 167–223, Jan. 2000.

[3] A. L. Velikovich, J. Davis, J. W. Thornhill, J. L. Giuliani, L. I. Rudakov, and C. Deeney, "Model of enhanced energy deposition in a Z-pinch plasma," *Phys. Plasmas*, vol. 7, no. 8, pp. 3265–3277, Aug. 2000.

[4] M. Sarfaty et al., "Spectroscopic investigations of the plasma behavior in a plasma opening switch experiment," *Phys. Plasmas*, vol. 2, no. 6, pp. 2122–2137, Jun. 1995.

[5] B. Rubinstein, R. Doron, Y. Maron, A. Fruchtman, and T. A. Mehlhorn, "The structure of a magnetic-field front propagating non-diffusively in low-resistivity multi-species plasma," *Phys. Plasmas*, vol. 23, no. 4, Apr. 2016, Art. no. 040703.

[6] S. N. Bland et al., "Use of Faraday probing to estimate current distribution in wire array Z pinches," *Rev. Sci. Instrum.*, vol. 77, no. 10, Oct. 2006, Art. no. 10E315.

[7] V. V. Ivanov et al., "UV laser-probing diagnostics for the dense Z pinch," *IEEE Trans. Plasma Sci.*, vol. 42, no. 5, pp. 1153–1162, May 2014.

[8] V. V. Ivanov et al., "Current redistribution and generation of kinetic energy in the stagnated Z pinch," *Phys. Rev. E, Stat. Phys. Plasmas Fluids Relat. Interdiscip. Top.*, vol. 88, no. 1, Jul. 2013, Art. no. 013108.

[9] M. Borghesi et al., "Proton imaging: A diagnostic for inertial confinement fusion/fast ignitor studies," *Plasma Phys. Controlled Fusion*, vol. 43, no. 12A, pp. A267–A276, Dec. 2001.

[10] C. K. Li et al., "Measuring E and B fields in laser-produced plasmas with monoenergetic proton radiography," *Phys. Rev. Lett.*, vol. 97, no. 13, Sep. 2006, Art. no. 135003.

[11] P. M. Nilson et al., "Magnetic reconnection and plasma dynamics in two-beam laser-solid interactions," *Phys. Rev. Lett.*, vol. 97, no. 25, Dec. 2006, Art. no. 255001.

[12] N. L. Kugland, D. D. Ryutov, C. Plechaty, J. S. Ross, and H.-S. Park, "Invited article: Relation between electric and magnetic field structures and their proton-beam images," *Rev. Sci. Instrum.*, vol. 83, no. 10, Oct. 2012, Art. no. 101301.

[13] D. Mariscal et al., "Measurement of pulsed-power-driven magnetic fields via proton deflectometry," *Appl. Phys. Lett.*, vol. 105, no. 22, Dec. 2014, Art. no. 224103.

[14] V. Munzar et al., "Mapping of azimuthal B-fields in Z-pinch plasmas using Z-pinch-driven ion deflectometry," *Phys. Plasmas*, vol. 28, no. 6, Jun. 2021, Art. no. 062702.

[15] Y. Maron, "Experimental determination of the thermal, turbulent, and rotational ion motion and magnetic field profiles in imploding plasmas," *Phys. Plasmas*, vol. 27, no. 6, Jun. 2020, Art. no. 060901.

[16] R. Doron et al., "Determination of magnetic fields based on the Zeeman effect in regimes inaccessible by Zeeman-splitting spectroscopy," *High Energy Density Phys.*, vol. 10, pp. 56–60, Mar. 2014.

[17] G. Davara, L. Gregorian, E. Kroupp, and Y. Maron, "Spectroscopic determination of the magnetic-field distribution in an imploding plasma," *Phys. Plasmas*, vol. 5, no. 4, pp. 1068–1075, Apr. 1998.

[18] L. Gregorian, V. A. Bernshtam, E. Kroupp, G. Davara, and Y. Maron, "Use of emission-line intensities for a self-consistent determination of the particle densities in a transient plasma," *Phys. Rev. E, Stat. Phys. Plasmas Fluids Relat. Interdiscip. Top.*, vol. 67, no. 1, Jan. 2003, Art. no. 016404.

[19] L. Gregorian et al., "Electron-temperature and energy-flow history in an imploding plasma," *Phys. Rev. E, Stat. Phys. Plasmas Fluids Relat. Interdiscip. Top.*, vol. 71, no. 5, May 2005, Art. no. 056402.

[20] M. E. Foord, Y. Maron, G. Davara, L. Gregorian, and A. Fisher, "Particle velocity distributions and ionization processes in a gas-puff Z pinch," *Phys. Rev. Lett.*, vol. 72, no. 24, pp. 3827–3830, Jun. 1994.

[21] L. Gregorian et al., "Electron density and ionization dynamics in an imploding Z-pinch plasma," *Phys. Plasmas*, vol. 12, no. 9, Sep. 2005, Art. no. 092704.

[22] R. P. Golingo, U. Shumlak, and D. J. Den Hartog, "Note: Zeeman splitting measurements in a high-temperature plasma," *Rev. Sci. Instrum.*, vol. 81, no. 12, Dec. 2010, Art. no. 126104.

[23] G. Mathys, "Spectropolarimetry of magnetic stars. II—The mean longitudinal magnetic field," *Astron. Astrophys. Suppl. Ser.*, vol. 89, no. 1, pp. 121–157, Jul. 1991.

[24] S. Ertmer et al., "Optical isolation of spectral lines emitted by sputtered tungsten in a weakly magnetized plasma," *J. Phys. B: At., Mol. Opt. Phys.*, vol. 54, no. 2, Jan. 2020, Art. no. 025401.

[25] F. C. Jahoda, F. L. Ribe, and G. A. Sawyer, "Zeeman-effect magnetic field measurement of a high-temperature plasma," *Phys. Rev.*, vol. 131, no. 1, pp. 24–29, Jul. 1963.

[26] N. J. Peacock and B. A. Norton, "Measurement of megagauss magnetic fields in a plasma focus device," *Phys. Rev. A, Gen. Phys.*, vol. 11, no. 6, pp. 2142–2146, Jun. 1975.

[27] E. A. McLean, J. A. Stamper, C. K. Manka, H. R. Griem, D. W. Droemer, and B. H. Ripin, "Observation of magnetic fields in laser-produced plasma using the Zeeman effect," *Phys. Fluids*, vol. 27, no. 5, pp. 1327–1335, May 1984.

[28] J. F. Seely, U. Feldman, N. R. Sheeley, S. Suckewer, and A. M. Title, "Magnetic field measurements based on the Zeeman splitting of forbidden transitions," *Rev. Sci. Instrum.*, vol. 56, no. 5, pp. 855–856, May 1985.

[29] T. Shikama and P. M. Bellan, "Development of a polarization resolved spectroscopic diagnostic for measurements of the vector magnetic field in the Caltech coaxial magnetized plasma jet experiment," *Rev. Sci. Instrum.*, vol. 84, no. 2, Feb. 2013, Art. no. 023507.

[30] D. Mikitchuk et al., "Effects of a preembedded axial magnetic field on the current distribution in a Z-pinch implosion," *Phys. Rev. Lett.*, vol. 122, no. 4, Jan. 2019, Art. no. 045001.

[31] G. Rosenzweig, E. Kroupp, A. Fisher, and Y. Maron, "Measurements of the spatial magnetic field distribution in a Z-pinch plasma throughout the stagnation process," *J. Instrum.*, vol. 12, no. 9, Sep. 2017, Art. no. P09004.

[32] G. Rosenzweig et al., "Local measurements of the spatial magnetic field distribution in a Z-pinch plasma during and near stagnation using polarization spectroscopy," *Phys. Plasmas*, vol. 27, no. 2, Feb. 2020, Art. no. 022705.

[33] Y. Maron et al., "Pressure and energy balance of stagnating plasmas in Z-pinch experiments: Implications to current flow at stagnation," *Phys. Rev. Lett.*, vol. 111, no. 3, Jul. 2013, Art. no. 035001.

[34] E. Kroupp et al., "Turbulent stagnation in a Z-pinch plasma," *Phys. Rev. E, Stat. Phys. Plasmas Fluids Relat. Interdiscip. Top.*, vol. 97, no. 1, Jan. 2018, Art. no. 013202.

[35] S. Davidovits and N. J. Fisch, "Sudden viscous dissipation of compressing turbulence," *Phys. Rev. Lett.*, vol. 116, no. 10, Mar. 2016, Art. no. 105004.

[36] S. Davidovits and N. J. Fisch, "A lower bound on adiabatic heating of compressed turbulence for simulation and model validation," *Astrophys. J.*, vol. 838, no. 2, p. 118, Mar. 2017.

[37] S. Davidovits and N. J. Fisch, "Bulk hydrodynamic stability and turbulent saturation in compressing hot spots," *Phys. Plasmas*, vol. 25, no. 4, Apr. 2018, Art. no. 042703.

[38] S. Davidovits and N. J. Fisch, "Modeling turbulent energy behavior and sudden viscous dissipation in compressing plasma turbulence," *Phys. Plasmas*, vol. 24, no. 12, Dec. 2017, Art. no. 122311.

[39] S. Davidovits and N. J. Fisch, "Compressing turbulence and sudden viscous dissipation with compression-dependent ionization state," *Phys. Rev. E, Stat. Phys. Plasmas Fluids Relat. Interdiscip. Top.*, vol. 94, no. 5, Nov. 2016, Art. no. 053206.

[40] Q. Tal, K. Eyal, and Y. Maron, "Radial current distribution of a gas-puff self imploding plasma close to stagnation," in *Proc. IEEE Int. Conf. Plasma Sci. (ICOPS)*, Singapore, Dec. 2020, p. 426.

[41] T. Queller et al., "Experimental investigation of the inductance of an imploding Z-pinch plasma column close to stagnation," in *Proc. IEEE Int. Conf. Plasma Sci. (ICOPS)*, Lake Tahoe, NV, USA, Sep. 2021, p. 1.

[42] V. Tangri, J. L. Giuliani, A. Dasgupta, T. Queller, E. Kroupp, and Y. Maron, "Recent simulations of nozzle gas flow and gas-puff Z-pinch implosions with magnetic fields in the Weizmann Z-pinch," in *Proc. IEEE Int. Conf. Plasma Sci. (ICOPS)*, Lake Tahoe, NV, USA, Sep. 2021, p. 1.

[43] C. Stollberg, "Investigation of a small-scale self-compressing plasma column," Ph.D. thesis, Weizmann Inst. Sci., Rehovot, Israel, 2019.

[44] C. Stollberg, "Study of a current loss at a Z-pinch stagnation due to fast current redistribution," in *Proc. IEEE Int. Conf. Plasma Sci. (ICOPS)*, Seattle, WA, USA, May 2022, pp. 1–2.

[45] C. Stollberg et al., "Observation of fast current redistribution in an imploding plasma column," *Phys. Rev. Lett.*, vol. 130, 2023, Art. no. 205101.

[46] S. V. Lebedev, F. N. Beg, S. N. Bland, J. P. Chittenden, A. E. Dangor, and M. G. Haines, "Snowplow-like behavior in the implosion phase of wire array Z pinches," *Phys. Plasmas*, vol. 9, no. 5, pp. 2293–2301, May 2002.

[47] S. V. Lebedev et al., "Physics of wire array Z-pinch implosions: Experiments at imperial college," *Plasma Phys. Controlled Fusion*, vol. 47, no. 5A, pp. A91–A108, May 2005.

[48] G. N. Hall et al., "Structure of stagnated plasma in aluminum wire array Z pinches," *Phys. Plasmas*, vol. 13, no. 8, Aug. 2006, Art. no. 082701.

[49] G. C. Burdiak et al., "Determination of the inductance of imploding wire array Z-pinches using measurements of load voltage," *Phys. Plasmas*, vol. 20, no. 3, Mar. 2013, Art. no. 032705.

[50] V. V. Ivanov, A. A. Anderson, D. Papp, A. L. Astanovitskiy, V. Nalajala, and O. Dmitriev, "Study of magnetic fields and current in the Z pinch at stagnation," *Phys. Plasmas*, vol. 22, no. 9, Sep. 2015, Art. no. 092710.

[51] E. M. Waisman, M. E. Cuneo, W. A. Stygar, R. W. Lemke, K. W. Struve, and T. C. Wagoner, "Wire array implosion characteristics from determination of load inductance on the Z pulsed-power accelerator," *Phys. Plasmas*, vol. 11, no. 5, pp. 2009–2013, May 2004.

[52] M. E. Cuneo et al., "Characteristics and scaling of tungsten-wire-array Z-pinch implosion dynamics at 20 MA," *Phys. Rev. E, Stat. Phys. Plasmas Fluids Relat. Interdiscip. Top.*, vol. 71, Apr. 2005, Art. no. 046406.

[53] N. A. Aybar et al., "Dependence of plasma-current coupling on current rise time in gas-puff Z-pinches," *IEEE Trans. Plasma Sci.*, vol. 50, no. 9, pp. 2541–2547, Sep. 2022.

[54] I. E. Ochs et al., "Current channel evolution in ideal Z pinch for general velocity profiles," *Phys. Plasmas*, vol. 26, no. 12, Dec. 2019, Art. no. 122706.

[55] J. Angel, E. Freeman, W. Potter, D. Hammer, and H. Team, "Zeeman polarization spectroscopy on gas puff Z-pinches," presented at the 63rd Annu. Meeting APS Division Plasma Phys., Pittsburgh, PA, USA, Nov. 2021.

[56] M. R. Gomez et al., "Magnetic field measurements via visible spectroscopy on the Z machine," *Rev. Sci. Instrum.*, vol. 85, no. 11, Nov. 2014, Art. no. 11e609.

[57] J. T. Banasek, J. T. Engelbrecht, S. A. Pikuz, T. A. Shelkovenko, and D. A. Hammer, "Measuring 20–100 T B-fields using Zeeman splitting of sodium emission lines on a 500 kA pulsed power machine," *Rev. Sci. Instrum.*, vol. 87, no. 11, Nov. 2016, Art. no. 11D407, doi: 10.1063/1.4958912.

[58] M. Cvejić et al., "Self-generated plasma rotation in a Z-pinch implosion with preembedded axial magnetic field," *Phys. Rev. Lett.*, vol. 128, no. 1, Jan. 2022, Art. no. 015001.

[59] E. Stambulchik, K. Tsigutkin, and Y. Maron, "Spectroscopic method for measuring plasma magnetic fields having arbitrary distributions of direction and amplitude," *Phys. Rev. Lett.*, vol. 98, no. 22, May 2007, Art. no. 225001.

[60] E. Stambulchik and Y. Maron, "A study of ion-dynamics and correlation effects for spectral line broadening in plasma: K-shell lines," *J. Quant. Spectrosc. Radiat. Transf.*, vol. 99, nos. 1–3, pp. 730–749, May 2006.

[61] H. R. Griem, *Spectral Line Broadening by Plasmas*. New York, NY, USA: Academic, 1974.

[62] S. Tessarin et al., "Beyond Zeeman spectroscopy: Magnetic-field diagnostics with Stark-dominated line shapes," *Phys. Plasmas*, vol. 18, no. 9, Sep. 2011, Art. no. 093301.

[63] K. D. Hahn et al., "Overview of self-magnetically pinched-diode investigations on RITS-6," *IEEE Trans. Plasma Sci.*, vol. 38, no. 10, pp. 2652–2662, Oct. 2010.

[64] M. D. Johnston et al., "Measuring plasma formation field strength and current loss in pulsed power diodes," Sandia Nat. Lab., Albuquerque, NM, USA, Tech. Rep. SAND2017-12565, 2017.

[65] B. V. Oliver, K. Hahn, M. D. Johnston, and S. Portillo, "Advances in high intensity e-beam diode development for flash X-ray radiography," *Acta Phys. Polonica A*, vol. 115, no. 6, pp. 1044–1046, Jun. 2009.

[66] S. G. Patel et al., "Zeeman spectroscopy as a method for determining the magnetic field distribution in self-magnetic-pinch diodes," *Rev. Sci. Instrum.*, vol. 89, no. 10, Oct. 2018, Art. no. 10D123.

[67] S. Biswas et al., "Shielding of the azimuthal magnetic field by the anode plasma in a relativistic self-magnetic-pinch diode," *Phys. Plasmas*, vol. 25, no. 11, Nov. 2018, Art. no. 113102.

[68] Y. Maron, E. Sarid, E. Nahshoni, and O. Zahavi, "Time-dependent spectroscopic observation of the magnetic field in a high-power-diode plasma," *Phys. Rev. A, Gen. Phys.*, vol. 39, no. 11, pp. 5856–5862, Jun. 1989.

[69] S. A. Slutz et al., "Pulsed-power-driven cylindrical liner implosions of laser preheated fuel magnetized with an axial field," *Phys. Plasmas*, vol. 17, no. 5, May 2010, Art. no. 056303.

[70] S. A. Slutz and R. A. Vesey, "High-gain magnetized inertial fusion," *Phys. Rev. Lett.*, vol. 108, no. 2, Jan. 2012, Art. no. 025003.

[71] M. R. Gomez et al., "Experimental demonstration of fusion-relevant conditions in magnetized liner inertial fusion," *Phys. Rev. Lett.*, vol. 113, no. 15, Oct. 2014, Art. no. 155003.

[72] P. F. Knapp et al., "Effects of magnetization on fusion product trapping and secondary neutron spectra," *Phys. Plasmas*, vol. 22, no. 5, May 2015, Art. no. 056312.

[73] T. J. Awe et al., "Observations of modified three-dimensional instability structure for imploding Z-pinch liners that are premagnetized with an axial field," *Phys. Rev. Lett.*, vol. 111, no. 23, Dec. 2013, Art. no. 235005.

[74] S. A. Sorokin, "Gas-puff liner implosion in the configuration with helical current return rods," *Plasma Phys. Rep.*, vol. 39, no. 2, pp. 139–143, Feb. 2013.

[75] N. Qi et al., "Gas puff Z-pinch implosions with external B_z field on COBRA," *AIP Conf. Proc.*, vol. 1639, pp. 51–54, Dec. 2014.

[76] D. Mikitchuk et al., "Mitigation of instabilities in a Z-pinch plasma by a preembedded axial magnetic field," *IEEE Trans. Plasma Sci.*, vol. 42, no. 10, pp. 2524–2525, Oct. 2014.

[77] L. Atoyan et al., "Helical plasma striations in liners in the presence of an external axial magnetic field," *Phys. Plasmas*, vol. 23, no. 2, Feb. 2016, Art. no. 022708.

[78] D. A. Yager-Elorriaga et al., "Discrete helical modes in imploding and exploding cylindrical, magnetized liners," *Phys. Plasmas*, vol. 23, no. 12, Dec. 2016, Art. no. 124502.

[79] A. G. Rousskikh et al., "Effect of the axial magnetic field on a metallic gas-puff pinch implosion," *Phys. Plasmas*, vol. 23, no. 6, Jun. 2016, Art. no. 063502.

[80] F. Conti et al., "Study of stability in a liner-on-target gas puff Z-pinch as a function of pre-embedded axial magnetic field," *Phys. Plasmas*, vol. 27, no. 1, Jan. 2020, Art. no. 012702.

[81] P. C. Campbell et al., "Stabilization of liner implosions via a dynamic screw pinch," *Phys. Rev. Lett.*, vol. 125, no. 3, Jul. 2020, Art. no. 035001.

[82] S. V. Lebedev, A. Frank, and D. D. Ryutov, "Exploring astrophysics-relevant magnetohydrodynamics with pulsed-power laboratory facilities," *Rev. Modern Phys.*, vol. 91, no. 2, Apr. 2019, Art. no. 025002.

[83] D. Mikitchuk, *Investigation of the Compression of Magnetized Plasma and Magnetic Flux*. Cham, Switzerland: Springer, 2019.

[84] N. Aybar et al., "Azimuthal magnetic field distribution in gas-puff Z-pinch implosions with and without external magnetic stabilization," *Phys. Rev. E, Stat. Phys. Plasmas Fluids Relat. Interdiscip. Top.*, vol. 103, no. 5, May 2021, Art. no. 053205.

[85] Y. V. Ralchenko and Y. Maron, "Accelerated recombination due to resonant deexcitation of metastable states," *J. Quant. Spectrosc. Radiat. Transf.*, vol. 71, nos. 2–6, pp. 609–621, Oct. 2001.

[86] A. L. Velikovich et al., "Force-free current flow in Z pinches imploded in an axial magnetic field," in *Proc. IEEE Int. Conf. Plasma Sci. (ICOPS)*, May 2017, p. 1.

[87] C. E. Seyler, "Axial magnetic flux amplification in Hall-magnetohydrodynamic simulations of externally magnetized Z-pinches," *Phys. Plasmas*, vol. 27, no. 9, Sep. 2020, Art. no. 092102.

[88] F. S. Felber et al., "Ultrahigh magnetic fields produced in a gas-puff Z pinch," *J. Appl. Phys.*, vol. 64, no. 8, pp. 3831–3844, Oct. 1988.

[89] F. S. Felber et al., "Compression of ultrahigh magnetic fields in a gas-puff Z pinch," *Phys. Fluids*, vol. 31, no. 7, pp. 2053–2056, Jul. 1988.

[90] A. V. Shishlov et al., "Formation of tight plasma pinches and generation of high-power soft X-ray radiation pulses in fast Z-pinch implosions," *Laser Phys.*, vol. 16, no. 1, pp. 183–193, Jan. 2006.

[91] M. Cvejic, D. Mikitchuk, E. Kroupp, R. Doron, and Y. Maron, "Measurement of magnetic field compression by imploding plasma," in *News and Reports from High Energy Density Generated by Heavy Ion and Laser Beams*, K. Weyrich and D. Hoffmann, Eds. Darmstadt, Germany: GSI Helmholtz Centre for Heavy Ion Research, GSI Report 2020-2, 2019, doi: 10.15120/GSI-2020-01321.

[92] C. W. Mendel and S. A. Goldstein, "A fast-opening switch for use in REB diode experiments," *J. Appl. Phys.*, vol. 48, no. 3, pp. 1004–1006, Mar. 1977.

[93] G. Cooperstein and P. F. Ottinger, "Fast opening vacuum switches for high-power inductive energy storage," *IEEE Trans. Plasma Sci.*, vol. PS-15, no. 6, pp. 629–634, Dec. 1987.

[94] R. W. Stinnett et al., "Plasma opening switch development for the Particle Beam Fusion Accelerator II (PBFA II)," *IEEE Trans. Plasma Sci.*, vol. PS-15, no. 5, pp. 557–563, Oct. 1987.

[95] B. V. Weber, R. J. Commisso, R. A. Meger, J. M. Neri, W. F. Oliphant, and P. F. Ottinger, "Current distribution in a plasma erosion opening switch," *Appl. Phys. Lett.*, vol. 45, no. 10, pp. 1043–1045, Nov. 1984.

[96] P. F. Ottinger, S. A. Goldstein, and R. A. Meger, "Theoretical modeling of the plasma erosion opening switch for inductive storage applications," *J. Appl. Phys.*, vol. 56, no. 3, pp. 774–784, Aug. 1984.

[97] D. D. Hinshelwood et al., "Long conduction time plasma erosion opening switch experiment," *Appl. Phys. Lett.*, vol. 49, no. 24, pp. 1635–1637, Dec. 1986.

[98] C. W. Mendel, M. E. Savage, D. M. Zagar, W. W. Simpson, T. W. Grasser, and J. P. Quintenz, "Experiments on a current-toggled plasma-opening switch," *J. Appl. Phys.*, vol. 71, no. 8, pp. 3731–3746, Apr. 1992.

[99] M. Sarfaty et al., "Spectroscopic investigation of fast (ns) magnetic field penetration in a plasma," *Phys. Plasmas*, vol. 2, no. 6, pp. 2583–2589, Jun. 1995.

[100] R. Shpitalnik, A. Weingarten, K. Gomberoff, Y. Krasik, and Y. Maron, "Observations of two-dimensional magnetic field evolution in a plasma opening switch," *Phys. Plasmas*, vol. 5, no. 3, pp. 792–798, Mar. 1998.

[101] A. Weingarten, R. Arad, Y. Maron, and A. Fruchtman, "Ion separation due to magnetic field penetration into a multispecies plasma," *Phys. Rev. Lett.*, vol. 87, no. 11, Aug. 2001, Art. no. 115004.

[102] R. Arad, K. Tsigutkin, Y. Maron, A. Fruchtman, and J. D. Huba, "Observation of faster-than-diffusion magnetic field penetration into a plasma," *Phys. Plasmas*, vol. 10, no. 1, pp. 112–125, Jan. 2003.

[103] R. Arad, K. Tsigutkin, Y. Maron, and A. Fruchtman, "Investigation of the ion dynamics in a multispecies plasma under pulsed magnetic fields," *Phys. Plasmas*, vol. 11, no. 9, pp. 4515–4526, Sep. 2004.

[104] R. Doron et al., "Plasma dynamics in pulsed strong magnetic fields," *Phys. Plasmas*, vol. 11, no. 5, pp. 2411–2418, May 2004.

[105] S. Kingsep, Y. V. Mohkov, and K. V. Chukbar, "Nonlinear skin effects in a plasma," *Sov. J. Plasma Phys.*, vol. 10, p. 495, 1984.

[106] A. V. Gordeev, A. S. Kingsep, and L. I. Rudakov, "Electron magnetohydrodynamics," *Phys. Rep.*, vol. 243, no. 5, pp. 215–315, Jul. 1994.

[107] A. Fruchtman, "Penetration and expulsion of magnetic fields in plasmas due to the Hall field," *Phys. Fluids B: Plasma Phys.*, vol. B3, no. 8, pp. 1908–1912, Aug. 1991.

[108] A. Fruchtman and K. Gomberoff, "Magnetic field penetration due to the Hall field in (almost) collisionless plasmas," *Phys. Fluids B: Plasma Phys.*, vol. B5, no. 7, pp. 2371–2377, Jul. 1993.

[109] J. D. Huba, J. M. Grossmann, and P. F. Ottinger, "Hall magnetohydrodynamic modeling of a long-conduction-time plasma opening switch," *Phys. Plasmas*, vol. 1, no. 10, pp. 3444–3454, Oct. 1994.

[110] A. Fruchtman and L. I. Rudakov, "Two-dimensional fast penetration of a magnetic field into a homogeneous plasma," *Phys. Rev. Lett.*, vol. 69, no. 14, pp. 2070–2073, Oct. 1992.

[111] S. B. Swanekamp, J. M. Grossmann, A. Fruchtman, B. V. Oliver, and P. F. Ottinger, "Particle-in-cell simulations of fast magnetic field penetration into plasmas due to the Hall electric field," *Phys. Plasmas*, vol. 3, no. 10, pp. 3556–3563, Oct. 1996.

[112] A. S. Richardson, J. R. Angus, S. B. Swanekamp, P. F. Ottinger, and J. W. Schumer, "Visualization of magnetic field penetration in multicomponent plasma," *IEEE Trans. Plasma Sci.*, vol. 42, no. 10, pp. 2552–2553, Oct. 2014.

[113] R. Doron et al., "Electron density evolution during a fast, non-diffusive propagation of a magnetic field in a multi-ion-species plasma," *Phys. Plasmas*, vol. 23, no. 12, Dec. 2016, Art. no. 122126.

[114] K. Tsigutkin et al., "Electric fields in plasmas under pulsed currents," *Phys. Rev. E, Stat. Phys. Plasmas Fluids Relat. Interdiscip. Top.*, vol. 76, no. 4, Oct. 2007, Art. no. 046401.

[115] R. Arad, K. Tsigutkin, Y. V. Ralchenko, and Y. Maron, "Spectroscopic investigations of a dielectric-surface-discharge plasma source," *Phys. Plasmas*, vol. 7, no. 9, pp. 3797–3807, Sep. 2000.

[116] A. V. Gordeev and T. V. Losseva, "Formation of a Z-pinch during electromagnetic compression of a nonquasineutral current filament," *Plasma Phys. Rep.*, vol. 29, no. 9, pp. 748–756, Sep. 2003, Art. no. 6592001.

[117] H. R. Strauss, R. Doron, R. Arad, B. Rubinstein, Y. Maron, and A. Fruchtman, "Magnetic field propagation in a two ion species planar plasma opening switch," *Phys. Plasmas*, vol. 14, no. 5, May 2007, Art. no. 053504.

[118] P.-A. Gourdain and C. E. Seyler, "Impact of the Hall effect on high-energy-density plasma jets," *Phys. Rev. Lett.*, vol. 110, no. 1, Jan. 2013, Art. no. 015002.

[119] P.-A. Gourdain et al., "The impact of Hall physics on magnetized high energy density plasma jets," *Phys. Plasmas*, vol. 21, no. 5, May 2014, Art. no. 056307, doi: 10.1063/1.4872022.

[120] A. S. Richardson, J. R. Angus, S. B. Swanekamp, I. M. Rittersdorf, P. F. Ottinger, and J. W. Schumer, "The effect of electron inertia in Hall-driven magnetic field penetration in electron-magnetohydrodynamics," *Phys. Plasmas*, vol. 23, no. 5, May 2016, Art. no. 052110, doi: 10.1063/1.4948715.

[121] A. S. Richardson, S. B. Swanekamp, S. L. Jackson, D. Mosher, and P. F. Ottinger, "Propagation speed, linear stability, and ion acceleration in radially imploding Hall-driven electron-magnetohydrodynamic shocks," *Phys. Plasmas*, vol. 25, no. 1, Jan. 2018, Art. no. 014504.